

FIELD SCALE RESERVOIR SIMULATION THROUGH A LATTICE  
BOLTZMANN FRAMEWORK

A Dissertation

by

ZACHARY ROSS BENAMRAM

Submitted to the Office of Graduate and Professional Studies of  
Texas A&M University  
in partial fulfillment of the requirements for the degree of

DOCTOR OF PHILOSOPHY

Chair of Committee,	Hadi Nasrabadi
Committee Members,	Eduardo Gildin
	Maria Barrufet
	Mike King
Head of Department,	Daniel Hill

August 2017

Major Subject: Petroleum Engineering

Copyright 2017 Zachary Ross Benamram

## ABSTRACT

The primary motivation of this work is to simulate the complex behavior of oil, gas and water as it flows through an unconventional reservoir. Unconventional reservoirs require hydraulic fracturing to provide the reservoir with conductive pathways for fluid to flow. Without fracturing the rock, the oil and gas would remain trapped in impermeable pore spaces. Unconventional reservoirs typically exhibit high heterogeneity in rock properties but also in fluid flow regimes. A simulation tool needs to be able to capture small scale rock heterogeneities, multiple flow regimes, and additional interaction physics between the rock and fluid.

In this dissertation, an alternative approach to modeling oil and gas reservoirs at the field scale is presented. Instead of a 'top down' paradigm, typical of classic reservoir simulation techniques (finite element, finite volume and finite difference methods), this work focuses on a 'bottom up' paradigm called the lattice Boltzmann method (LBM).

The LBM is a numerical discretization of the Boltzmann equation, in which a fluid is described as a distribution of particles, each with a unique velocity. The evolution of the distribution of particles is governed by a series of streaming and collision operations. The streaming operation translates the particle distribution through space. The collision operator describes how the particle distribution interacts with other distributions - through collision and a transfer of momentum. The collective behavior of small scale particle dynamics (streaming and collision steps) yield macroscopic fluid behavior in the large space and time scale limit.

## DEDICATION

To Bunny, Yehoshua, and Lilian.

## ACKNOWLEDGEMENTS

I would like to thank my advisors Dr. Hadi Narsdabadi and Dr. Eduardo Gildin for their guidance and support throughout this research. I would also like to thank Dr. Mike King and Dr. Maria Barrufet for serving as my committee members and for providing valuable insight, which has advanced this work.

I would also like to thank my research group - Alexander Tarakanov, Mohammad Al-Dossary, Kingsley Madiebo, Bikai Jin, Sheng Luo, Mehrdad Alfi, Qi Yang, Ran Bi, and David Higuera - for their discussions, contributions, and support.

Lastly, I thank my family and friends - Susan Ross, Avi Benamram, Josh Benamram, Charlie Benamram, Robert Ross.

# TABLE OF CONTENTS

	Page
ABSTRACT . . . . .	ii
DEDICATION . . . . .	iii
ACKNOWLEDGEMENTS . . . . .	iv
TABLE OF CONTENTS . . . . .	v
LIST OF FIGURES . . . . .	viii
1. INTRODUCTION: THE IMPORTANCE OF RESEARCH . . . . .	1
1.1 Description of the Industrial Problem . . . . .	2
1.2 Current Approaches to Problem . . . . .	3
1.3 The Approach to this Work . . . . .	3
1.4 Scope of Research . . . . .	4
1.5 Document Layout . . . . .	5
2. LATTICE BOLTZMANN METHOD FOR FLUID FLOWS . . . . .	6
2.1 The Particle Velocity Distribution Function . . . . .	6
2.2 The Lattice Boltzmann Equation . . . . .	7
3. A GENERALIZED LATTICE BOLTZMANN MODEL FOR FLUID FLOW IN POROUS MEDIA AT THE REV SCALE . . . . .	12
4. BOUNDARY CONDITIONS . . . . .	16
4.1 Well Boundary Conditions . . . . .	16
4.2 Reservoir Edge Boundary Conditions . . . . .	19
5. GOVERNING EQUATIONS AND CONVERSION BETWEEN PHYSI- CAL AND LATTICE SYSTEMS . . . . .	20
5.1 Lattice to Physical System Conversions: Dynamic Similarity . . . . .	20
6. HOMOGENOUS AND HETEROGENOUS WELL SIMULATION . . . . .	25

6.1	Homogenous Well Simulation Results . . . . .	25
6.2	Heterogenous Well Simulation Results . . . . .	27
7.	LOCAL GRID REFINEMENT . . . . .	30
7.1	Motivation: Grid Refinement for Fracture Modeling . . . . .	30
7.2	Grid Refinement Overview . . . . .	30
7.3	Grid and Temporal Refinement . . . . .	31
7.4	Convective Refinement for Flows in Porous Media . . . . .	33
7.4.1	Rescaling Physical Properties . . . . .	33
7.4.2	Rescaling the Distribution Function . . . . .	35
7.4.3	Coupling from Fine to Coarse Grid . . . . .	40
7.4.4	Coupling from Coarse to Fine Grid . . . . .	42
7.4.5	Grid Coupling Algorithm . . . . .	42
7.5	Convective Grid Refinement Results . . . . .	43
7.5.1	Convergence Analysis of a 2D Channel Steady State Flow . . . . .	43
7.5.2	2D Channel Steady State Flow Results . . . . .	44
7.5.3	Convergence Analysis of a 2D Channel Pseudo Steady State Flow . . . . .	50
7.5.4	2D Channel Pseudo Steady State Flow Results . . . . .	50
7.5.5	Convergence Analysis of Homogenous Well Simulation Results . . . . .	52
7.6	Diffusive Refinement . . . . .	55
7.6.1	Rescaling Forcing Terms . . . . .	55
7.6.2	Rescaling the Distribution Function . . . . .	56
7.7	Diffusive Grid Refinement Results . . . . .	62
7.7.1	Convergence Analysis of Homogenous Well Simulation Results . . . . .	62
8.	CONCLUSIONS AND FINAL REMARKS . . . . .	64
8.1	Discussion of Results . . . . .	65
8.2	Opportunities for Further Research . . . . .	66
8.2.1	Grid Refinement . . . . .	66
8.2.2	Two and Three Phase Porous Media Flow . . . . .	66
8.2.3	Parallelization of GLBM and Comparison with Finite Difference Run Times . . . . .	67
	REFERENCES . . . . .	69
	APPENDIX A. NON DIMENSIONALIZATION OF GOVERNING EQUATIONS . . . . .	75
A.1	Non Dimensionalization of the Generalized Navier-Stokes Equation . . . . .	75
A.2	Non Dimensionalization of the Continuity Equation . . . . .	76

APPENDIX B. MODIFIED ZOU-HE BOUNDARY FORMULATION . . . . .	78
APPENDIX C. SPE-10 PERMEABILITY AND POROSITY FIELD . . . . .	80
APPENDIX D. MODIFIED ZOU-HE BOUNDARY FORMULATION EX- TENDED . . . . .	81

## LIST OF FIGURES

FIGURE		Page
1.1	An SEM image of a Devonian shale sample [5]. . . . .	2
2.1	The Maxwell Boltzmann Distribution, where $T_1$ and $T_2$ represent two different system temperatures. The distribution indicates the most probable speed of a particle. Another way to view the distribution is the average speed of a fluid group. As the temperature of the system increases, the probability of higher particle velocities increases. . . . .	7
2.2	Two states of a system are pictured, before and after a collision event. Top: In the initial state, two distribution functions are located a distance away, each with a unique density distribution. Bottom: Once streaming has completed and the particle ensembles arrive at the same position, collision occurs and the combined distribution relaxes to a state of local equilibrium. . . . .	8
2.3	Top: The continuous Boltzmann distribution is discretized over a finite set of particle velocities. The red lines are the distribution functions associated with a discretized velocity. Bottom: The discretization process occurs over physical space. The volume to be simulated is sectioned into nodes. Each node has a set of velocities, pictured above as the discretized velocity space - D2Q9 (dimension 2, velocity 9). The continuous particle distribution (red) is mapped over the 2-dimensional velocity space to form a lattice distribution. . . . .	9
2.4	Left: Distributions prior to streaming. Center: Distributions after streaming. Right: Distributions after collision . . . . .	10
4.1	Pressure is interpolated from the boundary (red) to the nearest neighboring lattice nodes (yellow) at each time step. At these neighboring nodes, the density distribution functions are solved using a modified Zou-He Boundary Condition. . . . .	17



4.2	The area pictured in red is the non-computational regime wherein the boundary lies. The yellow nodes are the nearest neighboring nodes to the boundary. The arrows represent the distribution components that stream from areas not within the computational regime. These distributions are solved through a modified Zou-He boundary condition.	18
6.1	Simulation of homogenous well reservoir in Darcy flow. Left: Comparison plot between generalized LBM (line) and commercial simulation software (box). Right: Visualized pressure profile of well through production life of reservoir. Pressure measured in lattice units. . . . .	26
6.2	Simulation of heterogenous well reservoir in Darcy flow. Left: Comparison plot between generalized LBM (line) and commercial simulation software (box). Right: Visualized pressure profile of well in heterogenous medium through production life of reservoir. Pressure measured in lattice units. . . . .	28
7.1	A multi-grid technique for local grid refinement. Finer meshes are overlaid on top of coarser meshes. Streaming and collision step occur over both the coarse and fine meshes even in areas of overlap [44]. . .	31
7.2	A multi-domain technique for local grid refinement. Finer meshes are overlaid on top of coarser meshes. Streaming and collision step occur over both the coarse and fine meshes even in areas of overlap [44]. . .	32
7.3	Transition zone between coarse and fine meshes in the convective flow regime. The sites labeled 'copy from coarse to fine' are the sites where information from the coarse grid is rescaled to all fine sites in the marked zone. Sites labeled 'copy from fine to coarse' are the sites where information is rescaled from the fine sites located within the coarse sites. The transition zone is two coarse lattice sites wide. This is due to the linear relation between time and lattice spacing. Twice the resolution requires twice the time steps for convective flows. . . .	39
7.4	Above the dashed line is a 1 dimensional excerpt from Fig. 7.3. Below the dashed line, the fine and coarse lattices are made distinct to highlight the unknown distribution functions after each successive streaming step. . . . .	40
7.5	2D Channel Geometry. Grid is discretized into either a fine domain 200 x 100 lattice units or a coarse domain of 100 x 50 lattice units. The domain inlet is held at initial reservoir pressure and the outlet is held at 80% of the initial reservoir pressure. . . . .	44

7.6	A convergence test between two mesh sizes, for a flow approaching a steady state solution. The size of the two meshes differs by a factor of 2. The relative error of the pressure profile along the channel is measured. . . . .	45
7.7	Pressure profile and relative error plots of a transition mesh using Schema 0 are shown in Fig. (a) and (b). Each line represents the pressure profile at intervals of 100 iteration steps. . . . .	46
7.8	Pressure profile and relative error plots of a transition mesh using Schema 1 are shown in Fig.(a) and (b). Each line represents the pressure profile at intervals of 100 iteration steps. . . . .	47
7.9	Pressure profile and relative error plots of a transition mesh using Schema 2 are shown in Fig.(a) and (b). Each line represents the pressure profile at intervals of 100 iteration steps. . . . .	48
7.10	Pressure profile and relative error plots of a transition mesh using Schema 3 are shown in Fig.(a) and (b). Each line represents the pressure profile at intervals of 100 iteration steps. . . . .	49
7.11	Plot of recovery factors using a variety of mesh schemes. Schema 1 provides recovery factor results that are closest to expected result. . .	49
7.12	A convergence test between two mesh sizes, for a flow approaching a pseudo steady state solution. The size of the two meshes differs by a factor of 2. The relative error of the pressure profile along the channel is measured . . . . .	51
7.13	Pseudo steady state 2D channel flow. Fig. (a) shows how the pressure field of a multi-domain mesh reduces over time as the 2D channel is drained. Fig. (b) is a plot of the relative error in the pressure field along the channel between the multi-domain mesh and the coarse only mesh. . . . .	51
7.14	Geometry of a Homogenous Well Simulation. No flow boundaries along the edge of the domain. Constant pressure sink of 80% the initial reservoir pressure. . . . .	53
7.15	A convergence test between three mesh sizes, for a point source geometry approaching a pseudo steady state solution. The size of successively finer meshes differs by a factor of 2. The recovery factor of each simulation is measured. A divergence in expected solution results from a convective refinement scheme. . . . .	54

7.16	The transition zone between coarse and fine meshes in the diffusive flow regime. The sites labeled 'copy from coarse to fine' are the sites where distribution functions are scaled from the coarse grid to the fine grid. Sites labeled 'copy from fine to coarse' are the sites where information is scaled from the fine sites to coarse sites. The transition zone is three coarse lattice units wide. This is due to the squared relation in time and lattice spacing $\delta t \propto \delta x^2$ . Twice the resolution requires four times as many time steps for diffusive flows. . . . .	60
7.17	Above the dashed line is a 1D excerpt of a diffusive mesh. Below the dashed line is the fine and coarse lattice sites are separated to highlight the unknown distribution functions after each successive streaming step . . . . .	60
7.18	A convergence test between three mesh sizes, for a point source geometry approaching a pseudo steady state solution. The size of successively finer meshes differs by a factor of 2. The recovery factor of each simulation is measured. A constant offset in the expected solution forms as a result diffusive refinement. . . . .	62
C.0.1	SPE-10 Permeability (top) and porosity (bottom) data. Permeability values are scaled logarithmically for viewing. SPE-10 data is used to compare the generalized LBM with commercial simulation software. The 10th layer of the permeability and porosity field were used for simulation of 2D reservoir. . . . .	80

## 1. INTRODUCTION: THE IMPORTANCE OF RESEARCH\*

The shale revolution in the United States ushered in a new era of energy independence. Horizontal drilling and hydraulic fracturing techniques enabled previously uneconomical plays to be delivered at exceptional rates. However, one piece of the unconventional technology mix has not yet reached the maturity of its counterparts - unconventional reservoir simulation tools. Up until now, conventional techniques for reservoir simulation were modified to account for the hyperbolic decline rates seen in unconventional assets. These hyperbolic rates are the direct result of the relationship between the completions process (e.g. hydraulic fracture treatments) and the complex subsurface properties (e.g. fracture networks and nano-permeabilities). Decline curve analysis (DCA) and analog reservoirs are still the only acceptable methods of unconventional asset evaluation for the U.S. Securities and Exchange Commission [1]. Although DCA is a preferred method for oil and gas asset evaluations, the method itself requires constant revision as the play is produced. Therefore the method is susceptible to a large range of economic uncertainties. This underscores the under-development of reservoir simulation tools towards the application of shale oil and gas reservoirs and simultaneously the importance of finding alternative approaches.

The Holy Grail for the modern reservoir engineer is to develop a model that accurately captures the complex nature of the unconventional reservoir to provide accurate reserve estimates and production forecasts. The differences between conventional and unconventional reservoirs are vast, as explained by [2] and [3]. Any updates to reservoir simulation software must reflect this difference.

---

\*Reprinted with permission from “Field-wide Flow Simulation in Fractured Porous Media within Lattice Boltzmann Framework” by Z. Benamram, A. Tarakanov, H. Nasrabadi, and E. Gildin, 2016. *Advances in Water Resources*, 96, 170-179, Copyright 2016 by Elsevier.

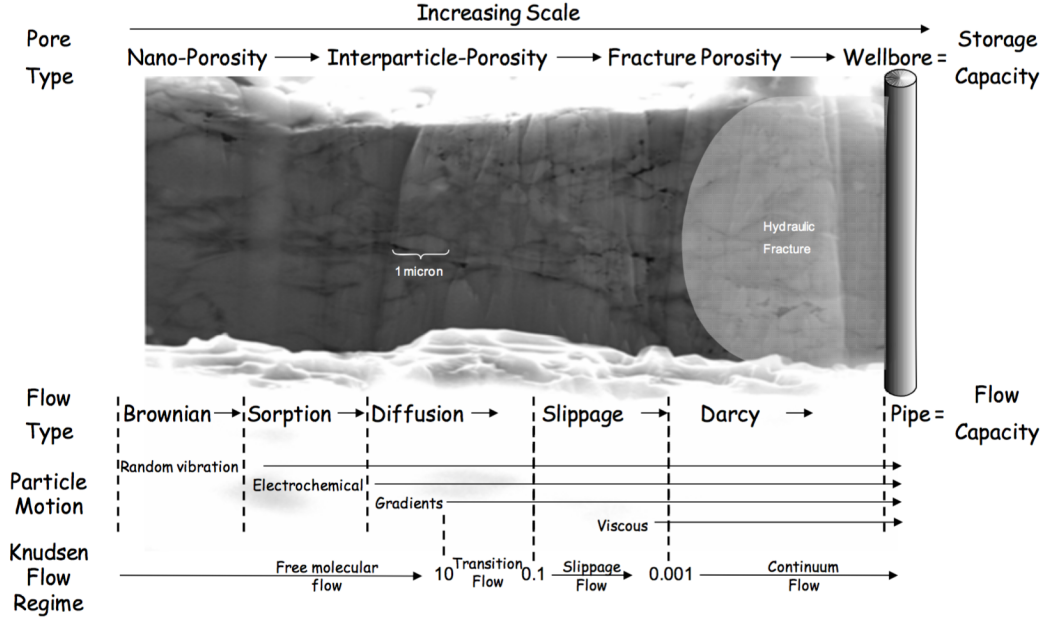


Figure 1.1: An SEM image of a Devonian shale sample [5].

## 1.1 Description of the Industrial Problem

The fractured reservoir system (FRS), distinct from the porous rock matrix, provides high conductive pathways for fluid flow. The majority of fluid production comes from these high conductive pathways and the neighboring porous matrix, and so, the geometry of the FRS is a primary indicator of future fluid production [3, 4]. Fig. 1.1 is an image of a Devonian shale gas sample, highlighting the various scales where hydrocarbons are stored [5].

The rate of production is also heavily dependent on the accelerating elements within the flow field. In reservoirs where fluid flows only through the porous rock matrix, Darcy flow is the primary flow regime [2]. However, in the FRS, inertial flows and non-linear damping flows play a significant part in the evolution of the flow field [6, 7, 8]. It is necessary, therefore, for a FRS simulation tool to address both the

complex boundary geometries and the multiple accelerating elements present in the flow field.

## 1.2 Current Approaches to Problem

Fluid flow in porous media at the field scale is most popularly modeled through finite element, finite volume, and finite difference methods [9].

To capture the cross flow between the porous rock matrix and the embedded fracture network, these methods incorporate single-porosity, dual-porosity, and discrete fracture models [10, 11, 12]. However, due to the challenges behind the implementation of these methods, and the high computational cost associated with capturing the geometry of the FRS, many in practice choose to idealize the fracture geometry [13, 14, 15].

## 1.3 The Approach to this Work

Instead of simulating the fractured reservoir system (FRS) within the finite element/volume/difference framework, we propose a different simulation paradigm for the FRS using the lattice Boltzmann method (LBM). The LBM has fundamental properties, which make the method an attractive alternative - including the ability to capture multiple flow regimes [16] as well as fine grained system resolution, while maintaining computational efficiency through simple parallelization procedures [17, 18]. Originally developed from the Lattice Gas Automata, the LBM has been successfully applied to fluid flow through porous medium at the pore scale [16]. However, sufficient pore geometry information is unavailable at the field scale, and so the LBM was modified to simulate flow over the representative volume element (REV) [19, 20, 21].

Most recently, Guo et al. [22] developed a generalized LBM (GLBM) for the simulation of isothermal incompressible porous flows at the REV scale. In comparison

to previous REV scale LBM, the GLBM includes convective accelerating elements in addition to linear and non-linear damping terms - perfect for the simulation of fluid flow through a FRS.

In this work, we extend the Guo et al. model to the FRS. To fully integrate the GLBM into a reservoir simulation tool, a GLBM FRS is proposed, which addresses the development of boundary conditions along the interface of the fracture network and the surrounding porous media. In addition, the GLBM FRS also provides a derivation of the governing dimensionless equations and a comprehensive methodology for the conversion between the lattice system and the physical system.

#### 1.4 Scope of Research

The aim of this research is to develop a LBM computational framework to simulate fluid flow in unconventional reservoirs. This same framework should also be able to model the correct physics within conventional reservoirs. Both two-dimensional and three-dimensional simulations will be considered.

The scope can be broken down into three components.

1. Implement the lattice Boltzmann method for fluid flow in porous media at the REV scale and validate performance against commercial reservoir simulation software for homogenous reservoir case.
2. Incorporate rock heterogeneities and compare implemented model with SPE-10, the collaborative solution project.
3. Develop local mesh refinement in LBM framework. Then investigate the effects of local grid refinement on numerical instabilities and compressibility effects inherent to the LBM.

## 1.5 Document Layout

The format of this paper is as follows: an overview of the LBM and the GLBM at the REV scale is given. We then will present the GLBM FRS. All derivations can be found in the appendices. Results for a homogenous and heterogenous reservoir are presented and validated against commercial reservoir simulation software. This is the first attempt to verify the GLBM in FRS against commercial reservoir simulation software. Last, we present a methodology for grid refinement.



## 2. LATTICE BOLTZMANN METHOD FOR FLUID FLOWS\*

Two approaches are employed in fluid simulations, commonly classified as bottom-up and top-down. In the top-down approach, the governing macroscopic fluid equations are discretized in time and space - what we referred to as a conventional simulation technique [9]. In the bottom-up approach, individual particles are tracked and their sum behavior represents macroscopic fluid properties. The lattice Boltzmann method is found to exist at a scale neatly between the two. The following section will provide an overview of the LBM. We will begin with the kinetic description of a fluid.

### 2.1 The Particle Velocity Distribution Function

A fluid is characterized as a collection of particles. The LBM treats this particle ensemble as a distribution function. The distribution states the amount of particles within the system associated with a specified velocity for all possible velocities. The Maxwell Boltzmann distribution, given by Eq. 2.1, provides the velocity distribution of a particle ensemble under the condition of point-like, structureless particles,

$$f(v) = \sqrt{\left(\frac{m}{2\pi kT}\right)^3} 4\pi v^2 e^{\frac{-mv^2}{2kT}} \quad (2.1)$$

where  $f$  is the particle distribution,  $v$  is the velocity,  $m$  is the particle mass, and  $KT$  is the product of the Boltzmann constant and system temperature [16] .

The Maxwell-Boltzmann distribution is both a probability distribution and also a density distribution. This difference in nomenclature arises from whether we apply

---

\*Reprinted with permission from “Field-wide Flow Simulation in Fractured Porous Media within Lattice Boltzmann Framework” by Z. Benamram, A. Tarakanov, H. Nasrabadi, and E. Gildin, 2016. Advances in Water Resources, 96, 170-179, Copyright 2016 by Elsevier.

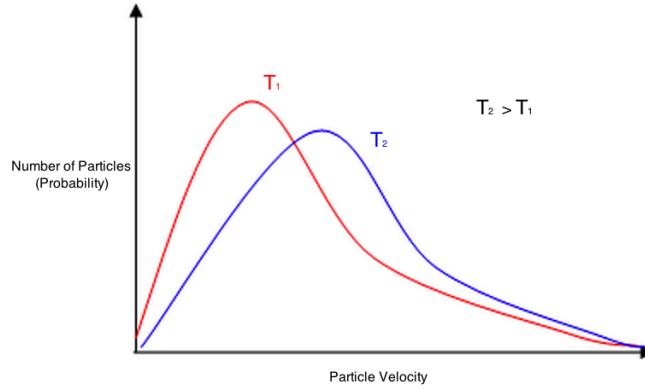


Figure 2.1: The Maxwell Boltzmann Distribution, where  $T_1$  and  $T_2$  represent two different system temperatures. The distribution indicates the most probable speed of a particle. Another way to view the distribution is the average speed of a fluid group. As the temperature of the system increases, the probability of higher particle velocities increases.

the distribution to a single particle or a group. In the case of a single particle, the Maxwell-Boltzmann distribution represents the most probable particle speed. For the case of an ensemble, the integral of the distribution function will yield the fluid density, shown in Fig. 2.1.

## 2.2 The Lattice Boltzmann Equation

The Boltzmann transport equation, shown in Eq. 2.2, is the time evolution of the distribution function [23].

$$D_t f = \left[ \partial_t + \frac{p}{m} \cdot \partial x + F \cdot \partial p \right] f(x, p, t) = \Omega \quad (2.2)$$

The evolution of the particle ensemble consists of streaming from one location to the next and the collision between other particle ensembles. The left hand side of the transport equation is the streaming step, or the spatial translation of the distribution function, under the influence of an external body force  $F$ , where  $p$  is the particle

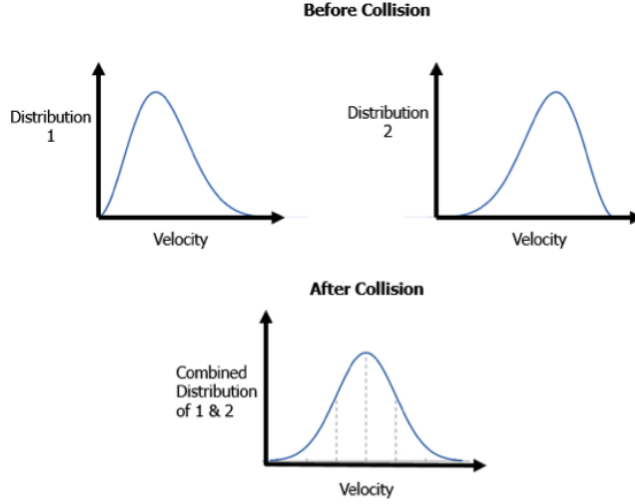


Figure 2.2: Two states of a system are pictured, before and after a collision event. Top: In the initial state, two distribution functions are located a distance away, each with a unique density distribution. Bottom: Once streaming has completed and the particle ensembles arrive at the same position, collision occurs and the combined distribution relaxes to a state of local equilibrium.

momentum. The right hand side shows the effect due to collision between particles,  $\Omega$ . Collision results in a transfer of momentum, also referred to as a relaxation to local equilibrium [24]. Fig. 2.2 is a visual representation of these interactions.

The lattice Boltzmann equation (LBE), shown in Eq. 2.3 is the first order discretization of the continuous Boltzmann transport equation.

$$f_i(x + e_i\delta_x, t + \delta_t) = f_i(x, t) - \frac{f_i(x, t) - f_i^{eq}(x, t)}{\tau} \quad (2.3)$$

Here, the collision term  $\Omega$  is approximated through a BGK operator [25]. This approximation states that the rate at which the streamed distribution function relaxes towards local equilibrium is governed by the relaxation parameter  $\tau$ . The subscript  $i$  indicates the direction associated with the D2Q9 lattice [16].

Next, the equilibrium distribution function is discretized over velocity space, given

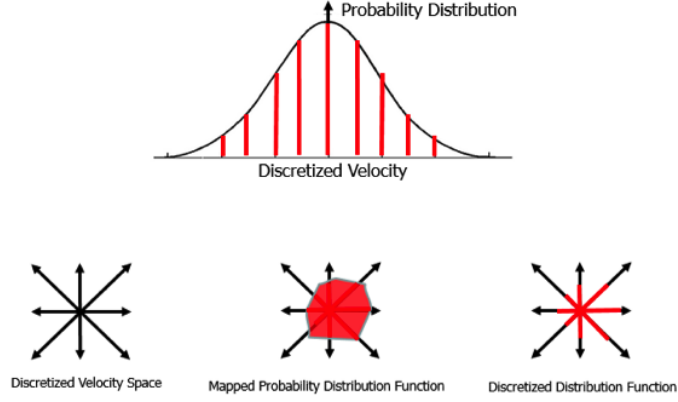


Figure 2.3: Top: The continuous Boltzmann distribution is discretized over a finite set of particle velocities. The red lines are the distribution functions associated with a discretized velocity. Bottom: The discretization process occurs over physical space. The volume to be simulated is sectioned into nodes. Each node has a set of velocities, pictured above as the discretized velocity space - D2Q9 (dimension 2, velocity 9). The continuous particle distribution (red) is mapped over the 2-dimensional velocity space to form a lattice distribution.

by Eq. 2.4.

$$f_i^{eq} = w_i \rho \left[ 1 + \frac{\mathbf{e}_i \cdot \mathbf{u}}{c_s^2} + \frac{\mathbf{u} \mathbf{u} : (\mathbf{e}_i \mathbf{e}_i - c_s^2 \mathbf{I})}{2c_s^4} \right] \quad (2.4)$$

where  $c_s$  is the speed of sound of the lattice and defined as  $c_s = \frac{\delta x}{\delta t} \frac{1}{\sqrt{3}}$ . Lattice velocities  $e_i$  and lattice weights  $w_i$  are chosen in accordance with the D2Q9 model, and given by Eq. 2.5 and 2.6.

$$\mathbf{e}_i = \begin{cases} 0 & i = 0 \\ (\cos(\frac{\pi}{2}(i-1)), \sin(\frac{\pi}{2}(i-1))) & i = 1 \dots 4 \\ \sqrt{2} (\cos(\frac{\pi}{4} + \frac{\pi}{2}(i-5)), \sin(\frac{\pi}{4} + \frac{\pi}{2}(i-5))) & i = 5 \dots 8 \end{cases} \quad (2.5)$$

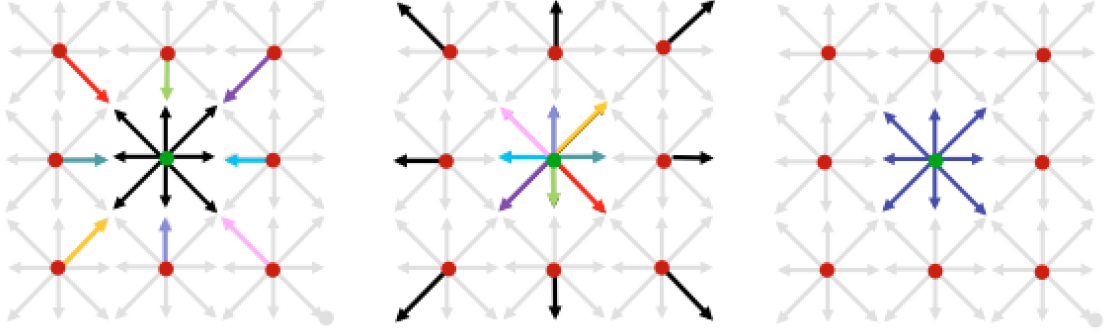


Figure 2.4: Left: Distributions prior to streaming. Center: Distributions after streaming. Right: Distributions after collision

$$w_i = \begin{cases} 4/9 & i = 0 \\ 1/9 & i = 1...4 \\ 1/36 & i = 5...8 \end{cases} \quad (2.6)$$

Fig. 2.4 attempts to show how the discretized distributions stream and collide. In the left most image, only the distribution functions which interact with the center node are shown. The black arrows are the discretized distribution functions of the center node. The colored arrows represent the distribution functions of the immediately neighboring nodes, which interact with the center node. The center image shows the the location of the distribution functions after streaming. As pictured, the distributions of the neighboring nodes (color) all meet at the center after translation, while the center node distribution functions have radiated outward. The right image represents the color distributions after collision has occurred. This collision shows the relaxation to local equilibrium. After the collision event occurs, the process repeats.

In order to calculate the distribution functions after the collision step, the volume averaged density and and velocity need to be calculated through Eq. 2.7.

$$\rho = \sum f_i, \quad \text{and} \quad \rho \mathbf{u} = \sum \mathbf{e}_i f_i \quad (2.7)$$

Through the Chapman-Enskog expansion, an unmodified LBE retains the Navier-Stokes Equation, given by Eq. 2.8, in the incompressible limit [26].

$$\frac{\partial(\rho \mathbf{u})}{\partial t} + \nabla \cdot \left( \frac{\rho \mathbf{u} \mathbf{u}}{\phi} \right) = -\nabla P + \nabla \cdot \left( \rho \nu_e (\mathbf{u} \nabla + \nabla \mathbf{u}) \right) \quad (2.8)$$

where  $P$  is the fluid pressure and  $\nu_e$  is the effective kinematic viscosity corresponding to the viscous stress that exists within the fluid itself (as opposed to kinematic viscosity  $\nu$ , which relates to the viscous stress near solid-liquid interfaces). We can group this equation into accelerating elements. The left hand side of Eq. 2.8 is the inertial element. The right hand side consists of the pressure and viscous elements.

In summary, fluid is treated as a statistical ensemble of point like particles, the time evolution of which is governed by a series of streaming and collision steps. Although many assumptions have been made in this kinetic description, it is proven in the macroscopic incompressible limit that the LBE retains the incompressible Navier-Stokes solution.

### 3. A GENERALIZED LATTICE BOLTZMANN MODEL FOR FLUID FLOW IN POROUS MEDIA AT THE REV SCALE\*

Soon after its emergence, the LBE was successfully applied to fluid flow at pore scales [27]. A primary advantage of the method is to simulate complex porous geometries without generating a complex lattice mesh. By adding more nodes within the same volume, the resolution of the boundary between solid and fluid nodes is enhanced. This benefit, coupled with a simple parallelization procedure of the LB algorithm, allows for the fast and accurate simulation of fluid flow through a complex geometry [28].

However, a detailed description of the pore geometry is unavailable over a large flow domain. Based on currently available measurement tools, only volume averaged rock properties (permeability and porosity) are obtainable. The representative volume element (REV) is the spatial extent over which this upscaling occurs [29]. Therefore, the Navier-Stokes equation is generalized to include empirically derived damping forces, which are a function of these volume averaged rock properties. Eq. 3.1 and 3.2 reflect the resistance to flow due the presence of porous medium.

$$\frac{\partial(\rho \mathbf{u})}{\partial t} + \nabla \cdot \left( \frac{\rho \mathbf{u} \mathbf{u}}{\phi} \right) = -\nabla P + \nabla \cdot \left( \rho \nu_e (\mathbf{u} \nabla + \nabla \mathbf{u}) \right) + \rho \mathbf{F} \quad (3.1)$$

$$\mathbf{F} = -\frac{\phi \nu}{K} \mathbf{u} - \frac{\phi F_e}{\sqrt{K}} |\mathbf{u}| \mathbf{u} + \phi \mathbf{G} \quad (3.2)$$

where  $F$  is the damping term,  $k$  is the permeability,  $\nu$  is the fluid viscosity due to

---

\*Reprinted with permission from “Field-wide Flow Simulation in Fractured Porous Media within Lattice Boltzmann Framework” by Z. Benamram, A. Tarakanov, H. Nasrabadi, and E. Gildin, 2016. Advances in Water Resources, 96, 170-179, Copyright 2016 by Elsevier.

shear between fluid and solid boundaries.  $F$  includes the linear in velocity Darcy term, the non-linear in velocity Forchheimer term and an external body force  $G$ . As  $\phi \rightarrow 1$  in the absence of porous media, the generalized Navier-Stokes equation reverts to the Navier-Stokes equation. At low flow velocities, the generalized Navier-Stokes equation reduces to Darcy flow, shown in Eq. 3.3.

$$\frac{\phi\nu}{K}\mathbf{u} = -\nabla P \quad (3.3)$$

Significant variations of permeability and porosity over small distances require that the REV be treated as small as possible. Natural and induced fractures add another layer of complexity in modeling flow. Fracture geometries require high spatial resolution. For similar reasons why the LBM is preferable over finite difference techniques in modeling fluid flow at the pore scale, a generalized LBM would be a suitable solution to model the REV scale.

Several LB models have been developed to simulate fluid flow through porous medium at the REV scale [19, 20, 21]. Selection of an optimal model should incorporate all relevant flow mechanisms, which govern fluid flow in a highly heterogeneous medium.

Within the LB framework, Guo et al. [22] proved through the Champman-Enskog expansion that the generalized Navier-Stokes equation can be obtained from a generalized lattice Boltzmann model (GLBM). To represent the presence of porous medium at every lattice node, the LBE is expanded to include a damping term, which is a function of the volume averaged permeability and porosity shown in Eq. 3.4 and 3.5.

$$f_i(x + e_i\delta_x, t + \delta_t) = f_i(x, t) - \frac{(f_i(x, t) - f_i^{eq}(x, t))}{\tau} + \delta_t F_i \quad (3.4)$$



$$F_i = w_i \rho \left( 1 - \frac{1}{2\tau} \right) \left[ \frac{\mathbf{e}_i \cdot \mathbf{F}}{c_s^2} + \frac{\mathbf{u} \mathbf{F} : (\mathbf{e}_i \mathbf{e}_i - c_s^2 \mathbf{I})}{\phi c_s^4} \right] \quad (3.5)$$

where the particle distribution functions  $f_i$  are treated as equilibrium distribution functions under the assumption of small deviation from local equilibrium [16].  $\mathbf{F}$  is the hydrodynamic damping force shown in Eq. 3.2. The discretized density distribution function is also altered to reflect the presence of a porous medium shown in Eq. 3.6.

$$f_i^{eq} = w_i \rho \left[ 1 + \frac{\mathbf{e}_i \cdot \mathbf{u}}{c_s^2} + \frac{\mathbf{u} \mathbf{u} : (\mathbf{e}_i \mathbf{e}_i - c_s^2 \mathbf{I})}{2\phi c_s^4} \right] \quad (3.6)$$

The equilibrium distribution function and the forcing term within the generalized LBE are both a function of the macroscopic fluid velocity. To solve for this unknown, the fluid velocity is defined by Eq. 3.7.

$$\rho \mathbf{u} = \sum \mathbf{e}_i f_i + \frac{\delta_t}{2} \rho \mathbf{F} \quad (3.7)$$

$F$  is also a function of  $\mathbf{u}$  and so Eq. 3.7 is non-linear with respect to velocity. Since the macroscopic velocity is quadratic, Eq. 3.7 can be re-written as Eq. 3.8.

$$\mathbf{u} = \frac{\mathbf{v}}{c_0 + \sqrt{c_0^2 + c_1 |\mathbf{v}|}} \quad (3.8)$$

where  $\mathbf{v}$  is termed the temporal velocity and defined in Eq. 3.9.

$$\rho \mathbf{v} = \sum e_i f_i + \frac{\delta_t}{2} \phi \rho \mathbf{G} \quad (3.9)$$

$c_0$  and  $c_1$  are shown in Eq. 3.10 and 3.11.

$$c_0 = \frac{1}{2} \left[ 1 + \phi \frac{\delta_t}{2} \frac{\nu}{K} \right] \quad (3.10)$$

$$c_1 = \phi \frac{\delta_t}{2} \frac{F_e}{\sqrt{K}} \quad (3.11)$$

The local density computation is identical to the unmodified LBM, where lattice density is equivalent to the summation of individual density distribution functions. In a supplementary article [30], Guo et al. shows how the governing macroscopic equations are retained through the Chapman-Enskog expansion in the incompressible limit. Through this analysis, equations of state are developed, shown in Eq. 3.12.

$$P = \frac{c_s^2 \rho}{\phi} \quad \text{and} \quad \nu_e = c_s^2 \left( \tau - \frac{1}{2} \right) \delta_t \quad (3.12)$$

## 4. BOUNDARY CONDITIONS\*

### 4.1 Well Boundary Conditions

Although high variations in permeability and porosity require the node to node length be minimized, the dimensions of the well and fracture are often smaller than the imposed unit node length. Therefore, it is often necessary to treat system boundaries with as few lattice nodes as possible. However, to retain the governing macroscopic flow equations through the Chapman-Enskog expansion, there must be sufficient node resolution to distinguish between the hydrodynamic and kinetic regimes [26]. The Chapman-Enskog analysis depends on the expansion through the smallness parameter, which is the ratio between the kinetic mean-free-path length and the hydrodynamic (smallest macroscopic) length. When the LBE simulates fluid flow over a few lattice nodes, there is no separation between the kinetic and hydrodynamic scales, calling the method's validity into question [31].

A low resolution boundary of the well and fracture boundary is achievable, however, through a combination of the damping term inherent to the GLBM and a modified Zou-He boundary condition applied to the well and fracture system. This section will contain the derivation and the procedure to apply a modified Zou-He boundary.

First, to establish the geometry of a constant pressure well and linear fracture, the boundary nodes should be set upon the nearest neighboring nodes of the boundary. In this way, the size of the well and the width of the fracture is incorporated. Pressure is interpolated linearly between the boundary and the nearest neighboring nodes

---

\*Reprinted with permission from "Field-wide Flow Simulation in Fractured Porous Media within Lattice Boltzmann Framework" by Z. Benamram, A. Tarakanov, H. Nasrabadi, and E. Gildin, 2016. *Advances in Water Resources*, 96, 170-179, Copyright 2016 by Elsevier.

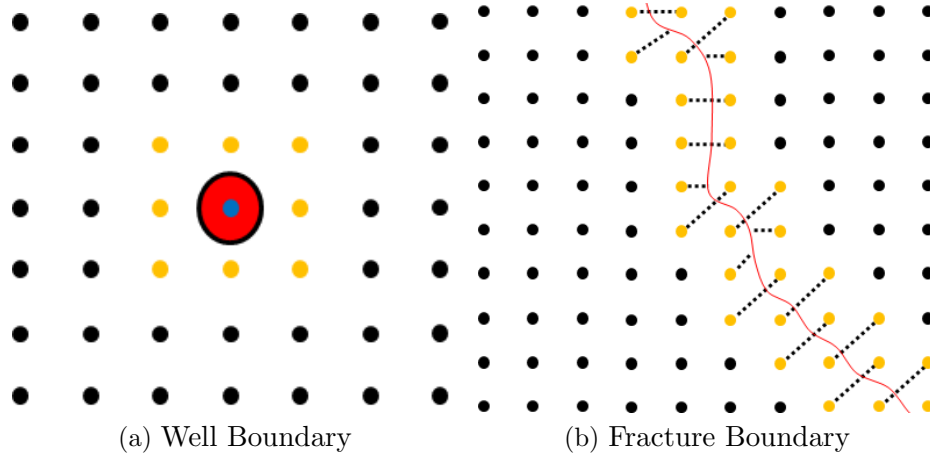


Figure 4.1: Pressure is interpolated from the boundary (red) to the nearest neighboring lattice nodes (yellow) at each time step. At these neighboring nodes, the density distribution functions are solved using a modified Zou-He Boundary Condition.

extending radially from the boundary, as shown in Fig. 4.1.

From the interpolated pressure, the lattice neighboring node density is calculated through an equation of state, given by Eq. 3.12. The interpolated density is used to solve for the unknown density distribution functions [32].

Pictured in Fig. 4.2 is the area in which the well and fracture boundary lies. On the face of these boundaries, a direct application of the Zo-He boundary condition will yield all unknown distributions that are in the direction of fluid flux. At the corner nodes of the fracture boundary, the flux is neither normal nor parallel to the containing boundary surfaces and therefore the Zou-He boundary must be modified to capture the distribution functions which are in the true direction of fluid flux.

As an example calculation, consider the bottom left corner node of the fracture in Fig. 4.2b. The unknown distribution functions,  $f_3$ ,  $f_4$ , and  $f_7$  are calculated in Eqs. 4.1, 4.2, and 4.3:

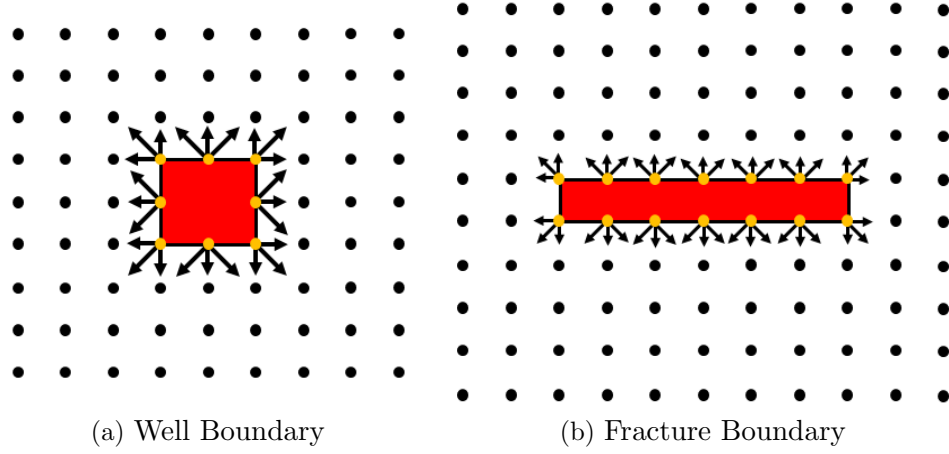


Figure 4.2: The area pictured in red is the non-computational regime wherein the boundary lies. The yellow nodes are the nearest neighboring nodes to the boundary. The arrows represent the distribution components that stream from areas not within the computational regime. These distributions are solved through a modified Zou-He boundary condition.

$$f_3 = f_1 + \frac{2}{5} \left( \rho - (f_0 + f_6 + f_8 + 2(f_1 + f_2 + f_5)) \right) + 2(f_6 - f_8) \quad (4.1)$$

$$f_4 = f_2 + \frac{2}{5} \left( \rho - (f_0 + f_6 + f_8 + 2(f_1 + f_2 + f_5)) \right) + 2(f_8 - f_6) \quad (4.2)$$

$$f_7 = f_5 + \frac{1}{5} \left( \rho - (f_0 + f_6 + f_8 + 2(f_1 + f_2 + f_5)) \right) \quad (4.3)$$

The full derivation of is found in Appendix B. We can apply the modified Zou-He boundary to the well for a more robust treatment of the unknown distribution functions of the well boundary.

To summarize, minimal node usage of the inner boundary is likely in the case of a sparse grid lattice configuration. There have been concerns over low resolution boundaries not respecting the Chapman-Enskog assumptions. In addition, low res-

olution boundaries can pose problems including the development of lattice effects (flow evolutions that are a result of the underlying grid geometry) [16]. A modified Zou-He boundary condition is established to counteract unrealistic flow evolutions and provide stable and accurate simulation results.

## 4.2 Reservoir Edge Boundary Conditions

Two outer boundary conditions are considered in reservoir simulation: the no-flow boundary condition and the constant pressure boundary condition. The no-flow boundary condition simulates a volumetric reservoir (no external sources of flow on the outer boundary). The constant pressure boundary simulates a reservoir that is bounded by another aquifer system.

Within the LB framework, a direct application of the Zou-He boundary condition on these outer nodes is sufficient. For the simulations posed in this paper, a no-flow boundary condition is used.

## 5. GOVERNING EQUATIONS AND CONVERSION BETWEEN PHYSICAL AND LATTICE SYSTEMS\*

The following two sections will provide the reader with a comprehensive methodology for applying the GLBM [30] towards the fractured reservoir system (FRS). Along with the GLBM itself, we must also consider the boundary conditions between the fracture network system and the porous media. In addition a consistent method for converting between the lattice system and the physical system must be established.

### 5.1 Lattice to Physical System Conversions: Dynamic Similarity

For two systems of different scales to exhibit identical flow evolutions, dynamic similarity must exist. Dynamic similarity ensures that two systems have identical length scale, time scale, and force scale ratios [33].

We will consider two geometries - the well and fracture. For the lattice system and physical system to exhibit geometric similarity, all three spatial dimension ratios of the reservoir as well as the ratio of well and fracture length to reservoir length must be identical.

A means to measure time scale and force scale ratios is by the non-dimensionalization of the generalized Navier-Stokes equation, through which the relative magnitudes of each force are compared. To derive the non-dimensional form of the generalized Navier Stokes equation, all flow dependent variables are substituted for a linear combination of the associated non-dimensional variables and characteristic system variables. A set of characteristic system parameters provide a constant measure of

---

\*Reprinted with permission from “Field-wide Flow Simulation in Fractured Porous Media within Lattice Boltzmann Framework” by Z. Benamram, A. Tarakanov, H. Nasrabadi, and E. Gildin, 2016. *Advances in Water Resources*, 96, 170-179, Copyright 2016 by Elsevier.

conversion between the physical and dimensionless systems. Typically, boundary conditions inform which parameters are suitable.

The characteristic length  $r_{0,p}$  is the physical distance from the inner boundary (well and fracture) to the edge of the reservoir. A second choice for the characteristic length is the node to node distance, or the resolution of the lattice, in physical units. The characteristic time  $t_{0,p}$  is chosen to be the fastest time scale for which a fluid can travel the characteristic length. This time scale occurs when the well is opened to production and exhibits the highest flow velocities, providing a bright line measurement for the characteristic velocity  $u_{0,p}$ . The characteristic time  $t_{0,p}$  can also be chosen for the time over which a boundary condition changes. The physical variables,  $r_p$ ,  $t_p$ , and  $u_p$  are listed in their dimensionless form as represented in Eq. 5.1.

$$r_d = r_p/r_{0,p}, \quad t_d = t_p/t_{0,p}, \quad u_d = u_p/u_{0,p} \quad (5.1)$$

Eq. 5.2 completes the set of dimensionless variables required for the nondimensionalization of the generalized Navier-Stokes equation.

$$\nabla_d = r_{0,p} \nabla_p, \quad \nabla_d^2 = r_{0,p}^2 \nabla_p^2, \quad P_d = \frac{P_p}{\mu_e \frac{u_{0,p}}{r_{0,p}}} \quad (5.2)$$

where the physical pressure is nondimensionalized by a characteristic viscous shear stress. The governing flow equation to be made dimensionless is an alternate form of the generalized Navier-Stokes equation, shown in Eq. 5.3, where only the Darcy term within the damping force is considered.

$$\frac{\partial \mathbf{u}}{\partial t} + \nabla \cdot \left( \frac{\mathbf{u}\mathbf{u}}{\phi} \right) = -\frac{1}{\rho} \nabla P + \nu_e \nabla^2 \mathbf{u} - \frac{\phi \nu}{K} \mathbf{u} \quad (5.3)$$



Eq. 5.3 shows five forcing elements: the time dependent term (variation), convection, diffusion, pressure, and damping in the order that they appear. A dimensionless form of the governing equation, shown in Eq. 5.4, is obtained by substituting the dimensionless variables found in Eq. 5.1 and 5.2. The full derivation can be found in Appendix A.1.

$$\frac{Re}{St} \frac{\partial u_d}{\partial t_d} + Re \nabla_d \cdot \frac{u_d u_d}{\phi} = -\nabla_d P_d + \nabla_d^2 u_d - \frac{\phi}{JDa} u_d \quad (5.4)$$

$$Re = \frac{u_{0,p} r_{0,p}}{\nu_e}, \quad J = \frac{\nu_e}{\nu}, \quad Da = \frac{K}{r_{0,p}^2} \quad (5.5)$$

$$\phi = \frac{\text{pore volume}}{\text{total volume}}, \quad St = \frac{t_{0,p} u_{0,p}}{r_{0,p}} \quad (5.6)$$

The final non-dimensionalized formulation shows that the evolution of the flow field is government by five dimensionless parameters - the Reynolds number  $Re$ , the Viscosity Ratio  $J$ , the Darcy Number  $Da$ , porosity  $\phi$  and the Strouhal number  $St$ .

In proposing the GLBM, Guo et al. mentioned only four non-dimensional parameters governing the evolution of the flow. Shown in the non-dimensional form of the generalized Navier-Stokes equation above, the Strouhal number is also a necessary component when considering the equivalency between physical and lattice systems. The Strouhal number is the ratio of the characteristic flow time scale,  $r_{0,p}/u_{0,p}$ , normalized by the reference time,  $t_{0,p}$ . If boundary conditions are changing quickly compared to the flow itself, which can be the case if the bottom-hole pressure rapidly drops, then the Strouhal number will highlight the difference in magnitude between the convective term and the temporal terms. For the purposes of the simulations posed in this paper, the boundary conditions are constant. Therefore, the Strouhal

number will be at unity.

To simulate Darcy flow, a choice in parameters must be made such that the magnitude of the Reynolds number is negligible, the Strouhal number is at unity and the combination of the Viscosity ratio and the Darcy number minimized. Under these conditions, the non-dimensionalized governing equation given in Eq. 5.4 reduces to the dimensionless Darcy equation, shown in Eq. 5.7.

$$\frac{\phi}{JDa} u_d = -\nabla_d P_d \quad (5.7)$$

We have determined a set of dimensionless parameters, which govern fluid flow evolution by nondimensionalizing the momentum balance equation. Let us apply the same technique to the continuity equation given by Eq. 5.8 for the case of an incompressible fluid with no sinks or sources.

$$\frac{\partial}{\partial t}(\rho\phi) = -\nabla \cdot (\rho u) \quad (5.8)$$

Eq. 5.9 is the dimensionless form of Eq. 5.8. The derivation can be found in Appendix A.2.

$$\frac{\partial}{\partial t_d} \rho_d = -\frac{1}{\phi} Da St \cdot \nabla^2(P_d) \quad (5.9)$$

The rate at which density changes over the flow field is proportional to the combined magnitude of the porosity, Darcy and the Strouhal number. This dimensionless grouping allows for a scaling of the characteristic time step. Any scale up to the characteristic time can be absorbed into the permeability term.

To conclude the discussion on dimensionless numbers, a mesoscopic description of a fluid can simulate identical flow evolutions to a system several orders of magnitude

in size larger by ensuring that the ratio of forces acting on a volume of fluid is identical and dynamic similarity is maintained.

## 6. HOMOGENOUS AND HETEROGENOUS WELL SIMULATION\*

### 6.1 Homogenous Well Simulation Results

The homogenous simulation inputs for the well and the fracture for both the LBM and commercial simulation are as follows: The reservoir is segmented into a 2D array of 200x200 nodes / grid blocks. The node to node distance (or length of the grid block) is 1m.

The fluid is treated as incompressible and the reservoir is fully saturated. Rock compressibility is omitted. The permeability  $k = 1$  darcy and porosity  $\phi$  is set at 20%.

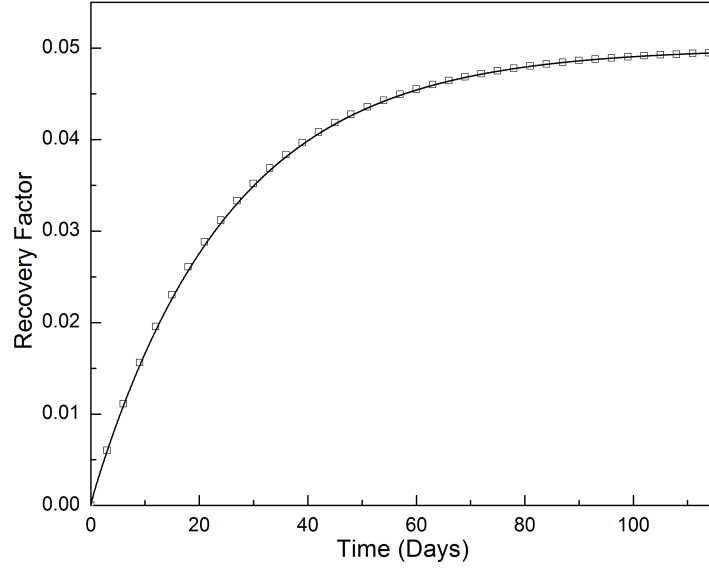
The diameter of the well is 0.2m set directly upon the center node. The fracture is treated as a line source positioned equidistantly from the surrounding nodes. Three fracture lengths are considered for simulation - 80m, 120m, and 160m.

The initial pressure of the reservoir is 100 kPa and the bottomhole flowing pressure is set to be 95% of the initial reservoir pressure. The inner boundary is treated as a constant pressure boundary and the edge of the reservoir maintains a no flow boundary condition. Refer to Section: *Lattice to Physical System Conversions: Dynamic Similarity* for converting physical parameters into lattice parameters.

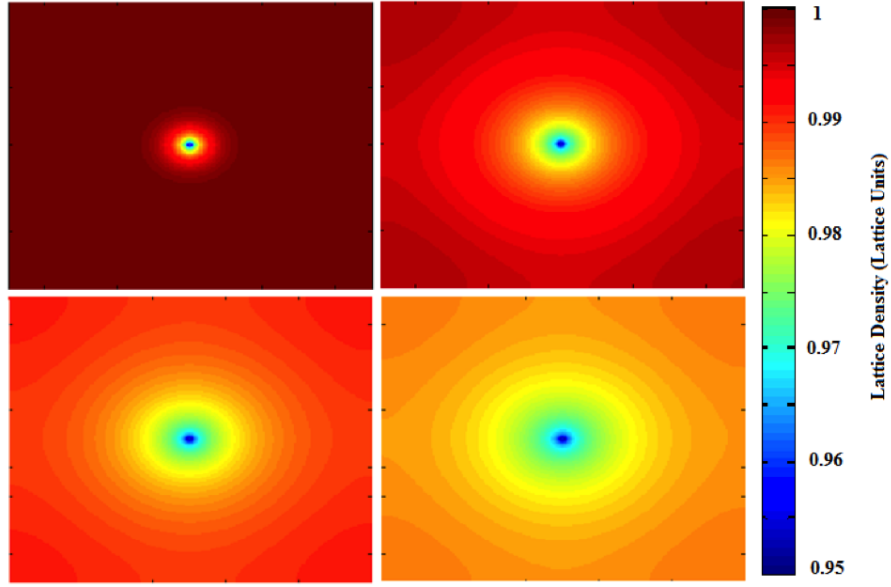
Fig. 6.1 shows the simulation results for a constant pressure well producing from a homogenous reservoir. These results are compared against the commercial simulation runs. The results are in excellent agreement for the case of Darcy flow.

---

\*Reprinted with permission from “Field-wide Flow Simulation in Fractured Porous Media within Lattice Boltzmann Framework” by Z. Benamram, A. Tarakanov, H. Nasrabadi, and E. Gildin, 2016. *Advances in Water Resources*, 96, 170-179, Copyright 2016 by Elsevier.



(a) Homogenous well result comparisons



(b) Homogenous well pressure profile

Figure 6.1: Simulation of homogenous well reservoir in Darcy flow. Left: Comparison plot between generalized LBM (line) and commercial simulation software (box). Right: Visualized pressure profile of well through production life of reservoir. Pressure measured in lattice units.

## 6.2 Heterogenous Well Simulation Results

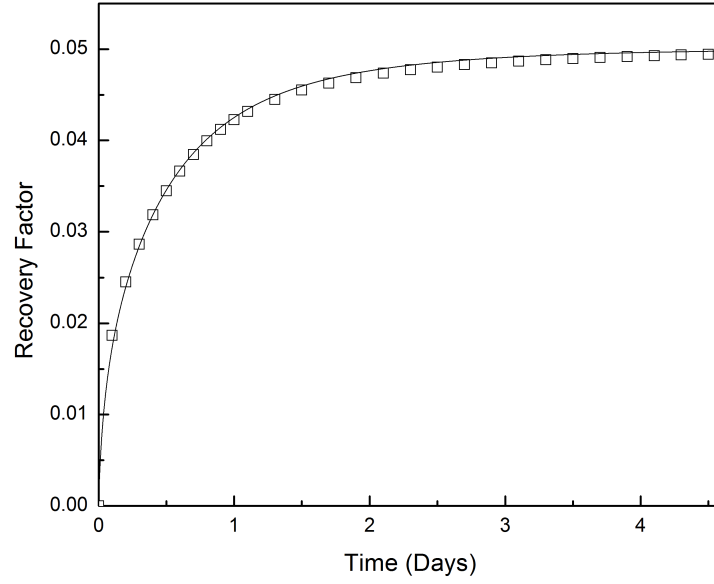
The heterogenous simulation inputs for the well case for both the LBM and commercial simulation are as follows: The reservoir is segmented into a 2D array of 220x60 nodes / grid blocks. The node to node distance (length of the grid block) is 3 m.

The fluid is treated as incompressible and the reservoir is fully saturated. Rock compressibility is omitted. The permeability and porosity arrays are taken from the 10th layer of the SPE-10 collaborative solution project, shown in Fig. C.0.1 in the Appendix [34]. The largest permeability value in the array is 2 Darcy and the minimum is  $3.8 \cdot 10^{-6}$  Darcy. The maximum porosity value is 48% and the minimum is 0%. However, the generalized equilibrium distribution function, given in Eq. 3.6, cannot take values porosity values of 0%. Therefore, all null values of porosity are treated as  $10^{-6}\%$ .

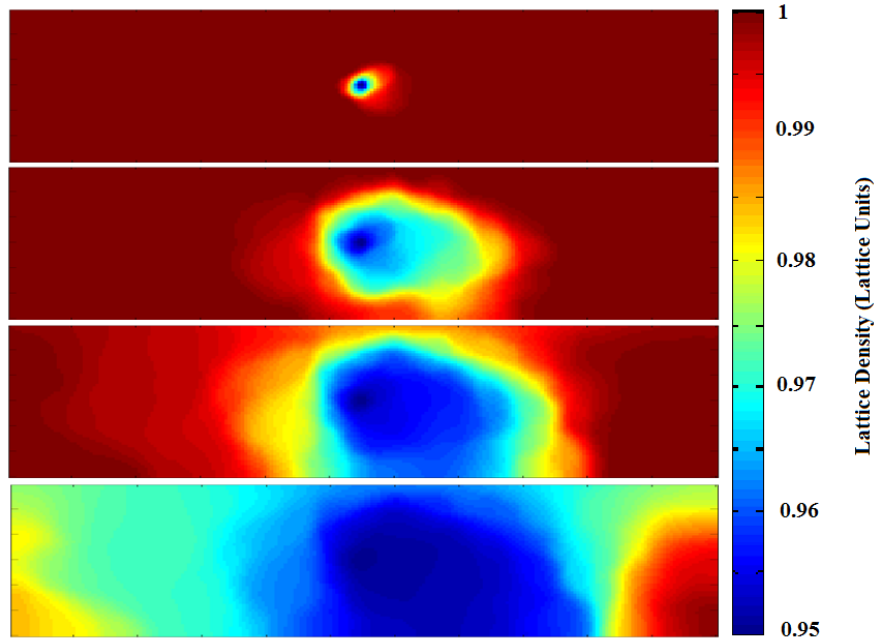
For well simulations, the diameter of the well is 0.2 m set in the center of the reservoir. The initial pressure of the reservoir is 100 kPa and the bottomhole flowing pressure is set to be 95% of the initial reservoir pressure. The inner boundary is treated as a constant pressure boundary and the edge of the reservoir maintains a no flow boundary condition. Refer to the methodology section for physical to lattice conversion methodology.

Fig. 6.2 shows the results for the simulation of fluid flow in a heterogenous porous material under production from a constant pressure well. The LBM results are compared against the commercial simulation results and show excellent agreement.

An interesting note: one of my concerns when developing the heterogenous model was implementing variations in permeability and porosity at the node level. The generalized naiver-stokes equation is only valid in the long wavelength long time limit.



(a) Heterogenous well result comparison



(b) Heterogenous well pressure profile

Figure 6.2: Simulation of heterogenous well reservoir in Darcy flow. Left: Comparison plot between generalized LBM (line) and commercial simulation software (box). Right: Visualized pressure profile of well in heterogenous medium through production life of reservoir. Pressure measured in lattice units.

What this means is that the generalized Navier-Stokes equation is not retained over a small domain of lattice nodes. We questioned whether variation in rock property at the node level would yield a deviating result from expected Darcy flow. What the results showed us was that this was not the case.



## 7. LOCAL GRID REFINEMENT

### 7.1 Motivation: Grid Refinement for Fracture Modeling

A constant pressure boundary condition along the surfaces of a fracture network is a common technique for modeling flows between a fracture network and the surrounding porous media [35, 36]. However, the use of a constant pressure boundary condition throughout the entirety of the fractured system is unphysical. The pressure response in the fracture is not instantaneous when the well is opened for production (i.e. the pressure response along a fracture is time dependent) [37]. This is why previous finite difference/volume/element and analytical models employ the concept of alternate permeability / porosity to simulate flow within a fracture [38, 39].

Refining the lattice mesh around the fracture zones into a high permeability fracture space is a useful technique. A locally mesh refined GLBM could simulate high Reynolds number and Forchheimer flows, while also capturing complex fracture geometry [22].

In addition, grid coarsening for the lattice Boltzmann method would improve the computational cost for simulation on a potentially dense lattice space [40, 41, 42]. For regions at the edge of the reservoir, where increasing reservoir resolution has a negligible effect on production rates / simulation results, grid coarsening reduces computational cost, while maintaining accuracy [43].

### 7.2 Grid Refinement Overview

There are two methods for local grid refinement: the multi-grid technique and the multi-domain technique [44, 45]. In the multi-grid technique, the coarse lattice mesh is present over the entire simulation domain, shown in Fig. 7.1.

The second method is the multi-domain technique. In the multi-domain ap-

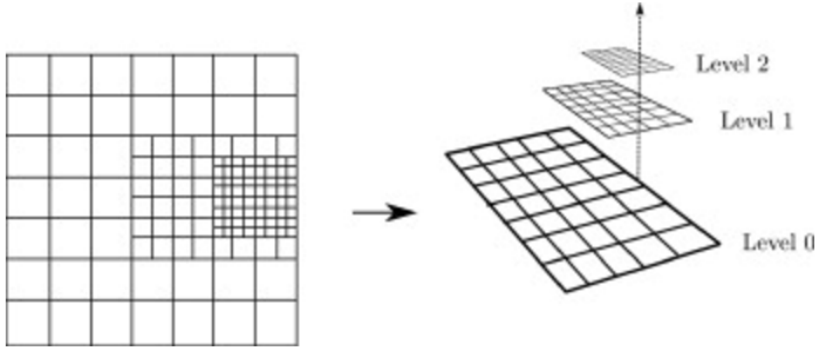


Figure 7.1: A multi-grid technique for local grid refinement. Finer meshes are overlaid on top of coarser meshes. Streaming and collision step occur over both the coarse and fine meshes even in areas of overlap [44].

proach, there is minimal overlap between coarse and fine meshes. Shown in Fig. 7.2, regions are not duplicated. The benefit is lower computational cost and memory usage at the expense of simplicity. One original motivation of using the LBM was efficiency and so a multi-domain approach aligns with this goal.

For this research, a local grid refinement scheme, developed by Lagrava et al. [44], is modified towards reservoir simulation at the field scale. The original Lagrava grid refinement scheme was for an unmodified lattice Boltzmann method, which simulated the Navier-Stokes equation. Because the GLBM is an extension of the LBM, modification is required to ensure dynamic similarity across transition zones.

### 7.3 Grid and Temporal Refinement

The choice in the level of grid refinement is application dependent but subject to increasing error as the ratio between successive grid refinement spacings increases [46]. For this discussion, the difference in scales between the coarse lattice mesh and fine lattice mesh is by a factor of 2.

$$\delta x_f = \delta x_c / 2 \quad (7.1)$$

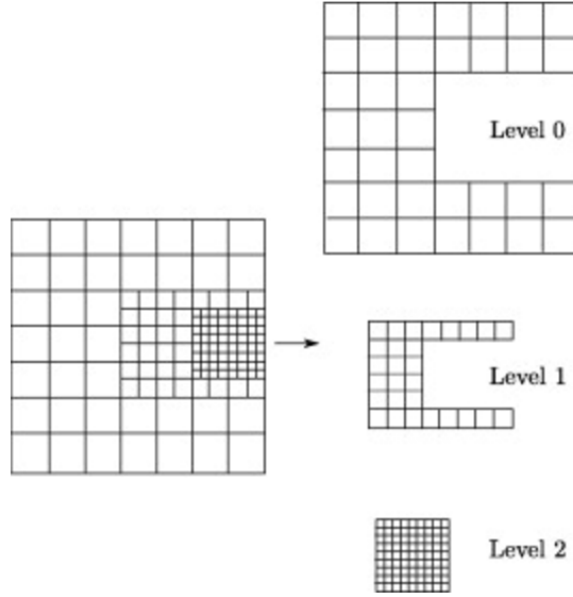


Figure 7.2: A multi-domain technique for local grid refinement. Finer meshes are overlaid on top of coarser meshes. Streaming and collision step occur over both the coarse and fine meshes even in areas of overlap [44].

where  $\delta x$  is the spacing between lattice sites.

The choice in temporal refinement is dependent on what are the dominating forcing elements within the flow field. Convective scaling and diffusive scaling are the most common temporal scaling operations. In convective scaling, the temporal scale is proportional to the spatial scale  $\delta t \propto \delta x$ . In diffusive scaling, the temporal scale is proportional to the square of the spatial scale,  $\delta t \propto \delta x^2$  [47].

If we inspect Eq. 2.8, we see that amongst the terms, there are differing relationships between the spatial and temporal scales. The advection terms exhibit a convective relation, while the viscous terms show a diffusive relation. And so depending on the flow regime of interest, the method by which the time step scales varies.

Since we simulate a mixed equation, in which diffusive, advective, and damping

forces are all present, a choice in either convective refinement or diffusive refinement wont work perfectly. In the sections following, a method for convective scaling in a multi-domain mesh is developed. We then explore how a convective refinement technique tests against a 2D channel flow and a 2D point source geometry. After, we discuss our work with diffusive grid refinement.

## 7.4 Convective Refinement for Flows in Porous Media

For two systems of differing dimensions to exhibit similar flow evolutions, dynamic similarity must be achieved. Mentioned previously in the discussion about dimensionless numbers, if two systems have similar geometries and the various forcing elements are in constant proportion to one another, both systems will exhibit similar flow evolution. This concept drives the development of a local refinement technique.

### 7.4.1 *Rescaling Physical Properties*

To understand how a scaling procedure of the LB equation is performed, we must identify how the particle distribution function and the forcing terms are spatially and temporally dependent. To ensure dynamic similarity, we must scale the distribution function and the magnitudes of the prevailing forces. Let us first consider how to scale the forcing terms, and then how to treat the distribution function itself.

#### 7.4.1.1 *Rescaling Forcing Terms*

Mentioned in previous sections, the governing parameters of a generalized Navier-Stokes equation are the Reynolds number, the Viscous number, the Darcy number, porosity, and the Strouhal number. To ensure dynamic similarity, these dimensionless quantities must be equivalent regardless of scale [33].

Let us first consider how scaling effects the viscous forces through examination

of the Reynolds number.

$$Re = \frac{U_n L_n}{\nu_{e_n}} \quad (7.2)$$

where the subscript n represents either a coarse or fine grid, and  $U_n$  and  $L_n$  are characteristic velocities and lengths of the system. The dimensionless numbers remain the same regardless of scale. Therefore, a relation can be made between the fine and coarse systems, shown in Eq. 7.3

$$Re_c = Re_f = \frac{UL\delta t_c}{\delta x_c^2 \nu_{e_c}} = \frac{UL\delta t_f}{\delta x_f^2 \nu_{e_f}} \quad (7.3)$$

$$\nu_{e_f} = \frac{\delta x_c}{\delta x_f} \nu_{e_c} \quad (7.4)$$

Given the equation above, we can now rescale the collision term,  $\tau$ :

$$\tau_c = \frac{1}{c_s^2} \frac{\delta x_f}{\delta x_c} \nu_{e_f} + \frac{1}{2} \quad (7.5)$$

or the converse:

$$\tau_f = \frac{1}{c_s^2} \frac{\delta x_c}{\delta x_f} \nu_{e_c} + \frac{1}{2} \quad (7.6)$$

Next, let us consider how scaling affects the damping effects due the presence of porous media. The Darcy number is defined and permeability is scaled in the following set of equations:

$$Da = K_n / L_n^2 \quad (7.7)$$

$$Da_c = Da_f = \frac{K_c}{L^2/\delta x_c^2} = \frac{K_f}{L^2/\delta x_f^2} \quad (7.8)$$

$$K_f = K_c \frac{\delta x_c^2}{\delta x_f^2} \quad (7.9)$$

The Viscous number is defined and viscosity is scaled using the scaling information provided by  $\tau$  scaling procedure in the Reynolds number section.

$$J = \frac{\nu_{en}}{\nu_n} \quad (7.10)$$

$$J_c = J_f = \frac{\nu_{ec}}{\nu_c} = \frac{\nu_{ef}}{\nu_f} \quad (7.11)$$

$$\nu_f = \frac{\nu_{ef}}{\nu_{ec}} \nu_c = \frac{\delta x_c}{\delta x_f} \nu_c \quad (7.12)$$

Last, porosity is scale independent and therefore does not change from the coarse system to the fine nor does it impact how the distribution function itself is rescaled.

To summarize, dimensionless numbers provide a method of conversion between coarse and fine system properties to ensure dynamic similarity.

#### 7.4.2 Rescaling the Distribution Function

Now that the forces are acting in constant proportion between a fine and coarse system, the next step is to develop a scheme for scaling the particle distribution function as it transitions from one mesh to another. But before we begin scaling the distribution function, let's quickly review the LBE itself.

A particle distribution function can be approximated by a Taylor expansion through the smallness parameter  $\varepsilon$ , shown in Eq. 7.13 [16].

$$f_i = f_i^{eq} + \varepsilon f_i^1 + \mathcal{O}(\varepsilon^2) \quad (7.13)$$

where  $\varepsilon$  is typically taken to be the ratio between mean free path of a particle and the smallest macroscopic length realized in the simulation. All higher order terms in Eq. 7.13 are small perturbations of the equilibrium distribution function, also referred to as the non-equilibrium components.

An explicit representation of the distribution function is given by Eq. 7.14.

$$f_i = w_i \rho \left[ 1 + \frac{\mathbf{e}_i \cdot \mathbf{u}}{c_s^2} + \frac{\mathbf{u} \mathbf{u} : (\mathbf{e}_i \mathbf{e}_i - c_s^2 \mathbf{I})}{2c_s^4} \right] - \frac{w_i \rho}{c_s^2 \omega} \mathbf{Q}_i : \mathbf{S} \quad (7.14)$$

$$\mathbf{Q}_i = \mathbf{e}_i \mathbf{e}_i - c_s^2 \mathbf{I} \quad (7.15)$$

$$\mathbf{S} = \frac{1}{2} \left[ \nabla \mathbf{u} + (\nabla \mathbf{u})^T \right] \quad (7.16)$$

The above explicit representation of the distribution function includes the equilibrium and non-equilibrium portions of the distribution function. The non-equilibrium portion is given by Eq. 7.15 and 7.16, which represents the shear strain rate of a fluid element acting upon its surroundings. By altering the temporal and spatial scales, we must consider how this changes the distribution function.

#### 7.4.2.1 Rescaling the Equilibrium Distribution Function

First, let us consider the equilibrium portion of the distribution function. The equilibrium portion of the distribution function in Eq. 7.14 is a function of lattice constants, fluid density, and a damped velocity. Lattice weights are grid format dependent (D2Q9 or D3Q19), and do not change under scaling. The speed of sound

of the lattice,  $c_s = \delta x / \delta t$  remains constant under convective scaling. Density is a continuous field on the lattice and so no scaling is required there either.

In the unmodified lattice Boltzmann scheme, velocity,  $v \propto \delta x / \delta t$ , goes unchanged during refinement. However, in the presence of porous media, velocity is damped. The magnitude of the damping is dependent on viscosity, time step, and the permeability of the formation and so therefore it is scale dependent. Damped velocity is given by Eq. 3.7 and the continuity of the damped velocity between fine and coarse grids is given by Eq. 7.17.

$$\frac{\mathbf{u}_c}{\mathbf{u}_f} = \alpha \quad (7.17)$$

where  $\alpha$  is the factor to be determined to impose continuity on the damped velocity field. If the terms in Eq. 7.17 are expanded using Eq. 3.7, we arrive at Eq. 7.18.

$$\frac{v_c}{1 + \phi \frac{\delta t_c}{2} \frac{\nu_c}{K_c}} = \alpha \frac{v_f}{1 + \phi \frac{\delta t_f}{2} \frac{\nu_f}{K_f}} \quad (7.18)$$

If the the temporal velocity terms are replaced with a characteristic velocity  $U$ , we get Eq. 7.19.

$$\frac{U \frac{\delta t_c}{\delta x_c}}{1 + \phi \frac{\delta t_c}{2} \frac{\nu_c}{K_c}} = \alpha \frac{U \frac{\delta t_f}{\delta x_f}}{1 + \phi \frac{\delta t_f}{2} \frac{\nu_f}{K_f}} \quad (7.19)$$

Through some algebraic manipulation we arrive at Eq. 7.20.

$$\alpha = \frac{\delta x_f}{\delta x_c} \frac{\delta t_c}{\delta t_f} + \frac{\delta x_f}{\delta x_c} \frac{\nu_f}{\nu_c} \frac{K_c}{K_f} \quad (7.20)$$

Through Eq. 7.20, an equivalency can be made between the equilibrium distribution function of the coarse and fine meshes, shown in Eq. 7.21 and 7.22.



$$f_{i,f}^{eq} = f_{i,c}^{eq}(\rho_c, \alpha \mathbf{u}_c) \quad (7.21)$$

$$f_{i,c}^{eq} = f_{i,f}^{eq}(\rho_f, \frac{1}{\alpha} \mathbf{u}_f) \quad (7.22)$$

#### 7.4.2.2 Rescaling the Non-Equilibrium Distribution Function

In previous work by Lagrava et al. [44], the non-equilibrium distribution function was scaled by creating an equivalency between the non-equilibrium portion of the distribution function of the fine and coarse meshes, shown in Eq. 7.23.

$$f_c^{neq} = \beta f_f^{neq} \quad (7.23)$$

Solving for  $\beta$  results in the following equations, shown in Eq. 7.24 and 7.25.

$$f_{i,f}^{neq} = \frac{\tau_f}{2\tau_c} f_{i,c}^{neq}(\mathbf{x}_c) \quad (7.24)$$

$$f_{i,c}^{neq} = \frac{2\tau_c}{\tau_f} f_{i,f}^{neq}(\mathbf{x}_f) \quad (7.25)$$

Combining the equilibrium and non-equilibrium scalings gives Eq. 7.26 and 7.27.

$$f_{i,f} = f_i^{eq}(\rho(\mathbf{x}_c), \alpha \mathbf{u}(\mathbf{x}_c)) + \frac{\tau_f}{2\tau_c} f_{i,c}^{neq}(\mathbf{x}_c) \quad (7.26)$$

$$f_{i,c} = f_i^{eq}(\rho(\mathbf{x}_f), \frac{1}{\alpha} \mathbf{u}(\mathbf{x}_f)) + \frac{2\tau_c}{\tau_f} f_{i,f}^{neq}(\mathbf{x}_f) \quad (7.27)$$

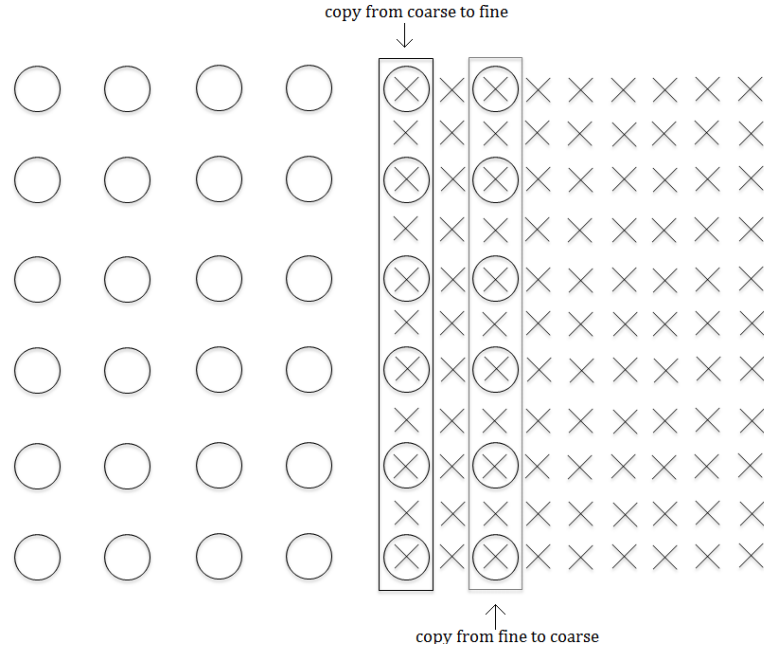


Figure 7.3: Transition zone between coarse and fine meshes in the convective flow regime. The sites labeled 'copy from coarse to fine' are the sites where information from the coarse grid is rescaled to all fine sites in the marked zone. Sites labeled 'copy from fine to coarse' are the sites where information is rescaled from the fine sites located within the coarse sites. The transition zone is two coarse lattice sites wide. This is due to the linear relation between time and lattice spacing. Twice the resolution requires twice the time steps for convective flows.

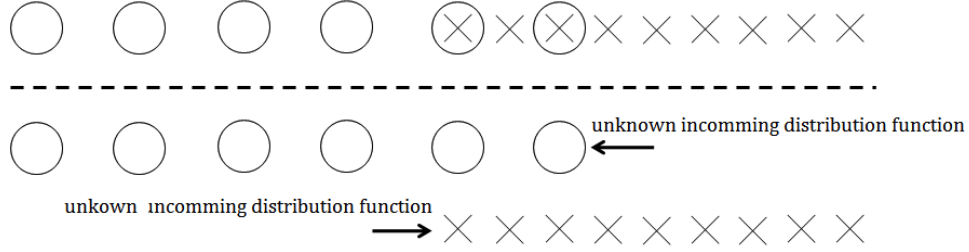


Figure 7.4: Above the dashed line is a 1 dimensional excerpt from Fig. 7.3. Below the dashed line, the fine and coarse lattices are made distinct to highlight the unknown distribution functions after each successive streaming step.

### 7.4.3 Coupling from Fine to Coarse Grid

The interface between the fine and coarse grids can be thought of conceptually as a boundary. Consider each individual mesh as a separate entity, shown in Fig. 7.3. At the edges of their domain, after the streaming step is completed, there are unknown distribution functions that have streamed from outside of the computational domain. The distribution functions from the adjacent meshes (fine or coarse) can be used to solve for these unknown distributions.

Let us first consider a 1D example, shown in Fig. 7.4. This 1D example is split into the coarse and fine components shown below the dashed line. The arrows indicate the unknown distribution functions for the one dimensional case.

There is an overlap between the meshes. This is so that at the end of the streaming step for each mesh, there will be unknown distribution functions to solve for at the boundary between the fine and coarse domains. If all the density and flow information is known at one scale, the scaling techniques shown previously can be applied to then solve for the unknown distribution functions at the other scale.

A few methods to solve for the unknown distribution functions along the boundary using scaled fluid and rock properties are shown in the subsequent sections.

#### 7.4.3.1 Schema 0: No scaling

What were to happen if no scaling was applied when solving for the unknown distribution functions? A simple copy and paste operation is performed on the distribution functions on the fine to the coarse site. This scheme is obviously incorrect based on the theory provided in earlier sections. It will be useful to show how drastically the effects of no scaling are on a final solution.

#### 7.4.3.2 Schema 1: Scaling Non-Equilibrium and Equilibrium Distributions

For all distribution functions on coarse nodes along the boundary of the coarse and fine domain, Eq. 7.27 is used. This method assumes that both the equilibrium and non-equilibrium portions of the distribution function contribute significantly to the evolution of the flow field.

#### 7.4.3.3 Schema 2: Scaling Equilibrium Distribution Only

Eq. 7.28 is used to solve for all coarse distribution functions along the boundary. This assumes that the non-equilibrium portion of the distribution function does not contribute to the evolution of the flow field.

$$f_{i,c} = f_{i,f}^{eq}(\rho_f, \frac{1}{\alpha} \mathbf{u}_f) \quad (7.28)$$

.

#### 7.4.3.4 Schema 3: Zou-He Scaling

The last method for solving for unknown distribution functions is an extension of the Zou-He boundary condition [32]. First, the velocity of fine grid nodes are scaled using Eq. 7.17. Then using the known density from the fine grid and the scaled damped velocity, all unknown distribution functions on the coarse grid can be solved

for using the Zou-He methodology.

#### 7.4.4 *Coupling from Coarse to Fine Grid*

The coupling process from the coarse grid to the fine grid is somewhat more complicated than rescaling from fine to coarse. Shown in Fig. 7.3, marked in the 'transition from coarse to fine' zone, there are two types of fine lattice nodes. The first type exist concurrently with the coarse nodes. The second type are adjacent to coarse nodes.

First, consider the fine lattice nodes that exist upon the coarse lattice nodes within the transition zone. Mentioned previously, two time steps occur in the fine mesh for every one time step in the coarse mesh in a convective refinement scheme. At time step  $t + \delta t_f$  on the fine mesh, a temporal interpolation is performed to solve for the density and velocity of the coarse mesh. For the fine sites that are not on coarse sites, a spatial interpolation step is also required. The damped velocity of the coarse mesh is rescaled using Eq. 7.17. Once the density and the damped velocity are known on the fine sites, we can employ any scheme shown in the previous section depending on the requirements of the application.

At time step  $t + 2\delta t_f$ , a temporal interpolation is not needed, since the nodal information is available from the coarse nodes sites. A spatial interpolation is still required for fine nodes not align with coarse nodes. Once the damped velocity is scaled, any scheme appropriate to the application can be used.

#### 7.4.5 *Grid Coupling Algorithm*

The Lagrava et al. [44] grid coupling algorithm is used for GLBM multi-domain meshes. Below are the steps required to pass information between meshes using the theory provided in previous sections.

1. A collide and stream operation is performed on the coarse grid, bringing the

time to  $t + \delta t_c$ . At this time, distributions at coarse nodes that were supposed to stream from the fine grid are unknown.

2. A collide and stream operation is performed on the fine grid, bringing the time to  $t + \delta t_c/2$ . The grid lacks information at the transition sites from coarse to fine. A double interpolation is performed (time and space). First  $\mathbf{u}_c$  is scaled using 7.17. Then the values of  $\rho_c$  and  $\mathbf{u}_f$  of the coarse sites are interpolated at time  $t + \delta t_c/2$ . Then the time interpolated values, are interpolated in space to fine nodes that are not overlaid on coarse node sites. All distribution functions are solved using a schema appropriate to the application.
3. On the next collide and stream operation, the time is brought to  $t + \delta t_c$ . No time interpolation is required during this step. Values for density and velocity are taken from step 1 and the velocity is scaled. A spatial interpolation is still required for off-coarse-node fine node lattice sites.
4. All populations of the coarse grid are updated using the schema of choice.

## 7.5 Convective Grid Refinement Results

### 7.5.1 Convergence Analysis of a 2D Channel Steady State Flow

We test for convergence of the solution by comparing the evolution of the flow field at successive levels of grid refinement. Increasing the resolution of the lattice reduces discretization errors. However, reducing the lattice size also has the consequence of increasing the compressibility error of the lattice Boltzmann method [16]. The compressibility error stems from the flow velocity approaching the speed of sound of the lattice. This is common in regions of high pressure differentials.

Flow parameters used are a relaxation factor used for the coarse grid was  $\tau_c = 2$ , the viscous number  $J = 1$ , the darcy number  $Da = 1$  and  $\phi = 1/4$ . The inlet is held

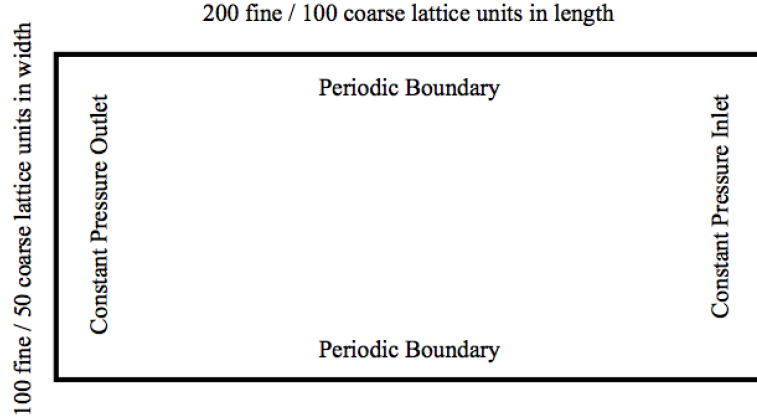


Figure 7.5: 2D Channel Geometry. Grid is discretized into either a fine domain 200 x 100 lattice units or a coarse domain of 100 x 50 lattice units. The domain inlet is held at initial reservoir pressure and the outlet is held at 80% of the initial reservoir pressure.

at 0.8 of the reservoir pressure and the outlet is held at the initial reservoir pressure.

The fine mesh is discretized into a 100 x 200 node domain. The coarse mesh is discretized into a 50 x 100 node domain. The relative error is computed between the coarse and the fine domains. The flow geometry is shown in Fig. 7.5.

Fig. 7.6 shows the results of a convergence test for a 2D channel under a constant pressure differential at the inlet and outlet. The convergence tests show that convective refinement yields a small error in the pressure profile along the channel. Now that there is similarity between coarse and fine grid solutions, a multi-domain scheme can be implemented for the 2D channel.

### 7.5.2 2D Channel Steady State Flow Results

To test the multi-domain grid refinement technique, a coarse and a fine domain are established along the channel, similar to what is shown in Fig. 7.3. The total distance along the channel is equivalent to 100 coarse lattice units long. A fine

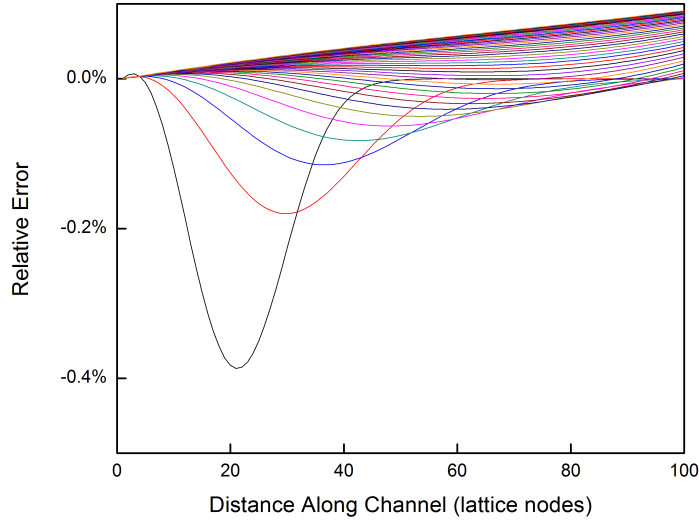


Figure 7.6: A convergence test between two mesh sizes, for a flow approaching a steady state solution. The size of the two meshes differs by a factor of 2. The relative error of the pressure profile along the channel is measured.

domain occupies the first half of the channel (100 fine lattice units) and a coarse mesh occupies the second half of the channel (51 lattice units). An overlap of 1 coarse lattice unit is applied. The flow and boundary parameters are kept from the convergence test.

The evolution of the pressure field in the multi-domain grid using Schema 0 is presented in Fig. 7.7. The transition zone occurs at the 49th and 51st lattice node along the channel.

As expected, when the simulation is allowed to run, a steady state condition is reached, shown by the convergence of the pressure profiles in Fig. 7.7a. As a consequence of Schema 0 not ensuring continuity, the pressure profile along the channel does not become linear over time. Instead, a kink is formed in the pressure profile. This is indicative of two flow regimes that are not in dynamic similarity.



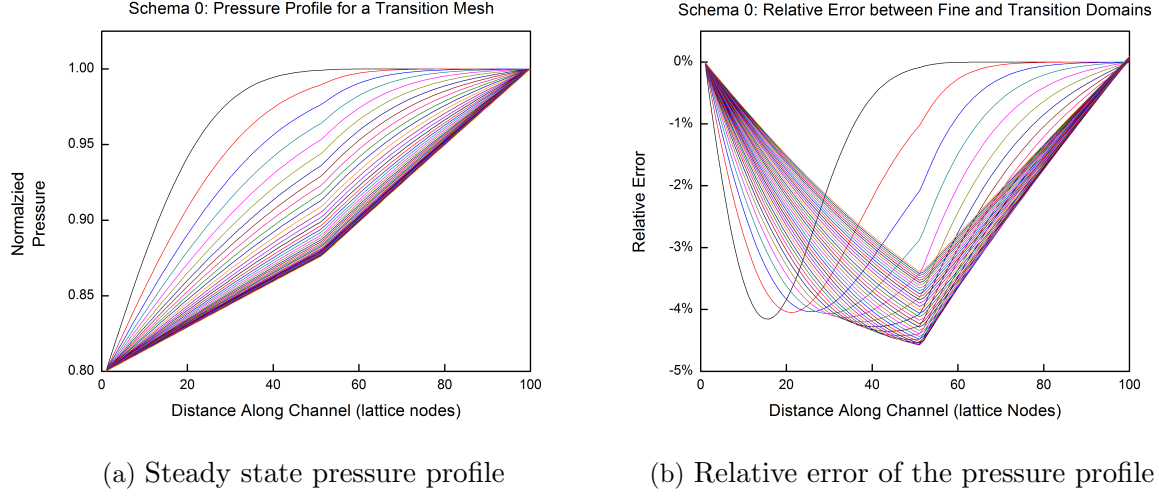


Figure 7.7: Pressure profile and relative error plots of a transition mesh using Schema 0 are shown in Fig. (a) and (b). Each line represents the pressure profile at intervals of 100 iteration steps.

To measure the accuracy of the multi-domain technique, a comparison is made between the pressure profiles of a fine only domain and a multi-domain. Fig. 7.7b plots the relative error calculated by Eq. 7.29. The maximum error is nearly 5%. This error will become worse in systems that are not symmetric perpendicular to the direction of flow.

$$error = \frac{P_{multi-domain} - P_{fine-domain}}{P_{fine-domain}} \quad (7.29)$$

The second scheme to be tested, Schema 1, follows the theory established of scaling the equilibrium and non-equilibrium distribution functions according to a convective refinement scheme. Fig. 7.8a shows how treating the transition zone in this manner produces the expected linear steady state solution along a channel.

The relative error for Schema 1 is shown in Fig. 7.8b. The error for a steady state solution is bounded between -0.8% and 0.2%. Max error occurs during early

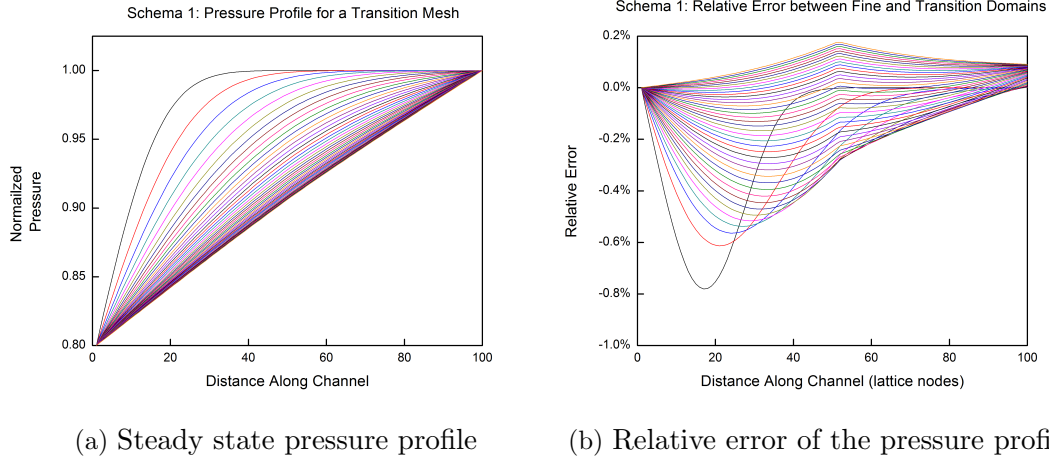


Figure 7.8: Pressure profile and relative error plots of a transition mesh using Schema 1 are shown in Fig.(a) and (b). Each line represents the pressure profile at intervals of 100 iteration steps.

times when the pressure boundary front first advances through the domain. Once the pressure front interacts with the constant pressure boundary held at the outlet, the relative error begins to lessen.

Schema 2 is based on the assumption that diffusive terms do not contribute significantly to the evolution of the flow field. Diffusive forces are essential in domains where a significant number of nodes are not aligned with the source/sink boundary. Diffusive forces allow for those nodes that are not aligned with the boundary to receive contributions. Given the 2D channel geometry presented for this simulation, where a periodic boundary condition is maintained along the top and bottom boundaries, and the inlet boundary is in line with every node in the domain, it is fair hypothesis to assume that diffusion does not play a significant role. Fig. 7.9 are the results of that hypothesis.

Shown in Fig. 7.9a, a kink forms early in the pressure profile and becomes distinct at later times. This shows that mass is not being conserved under Schema 2. As

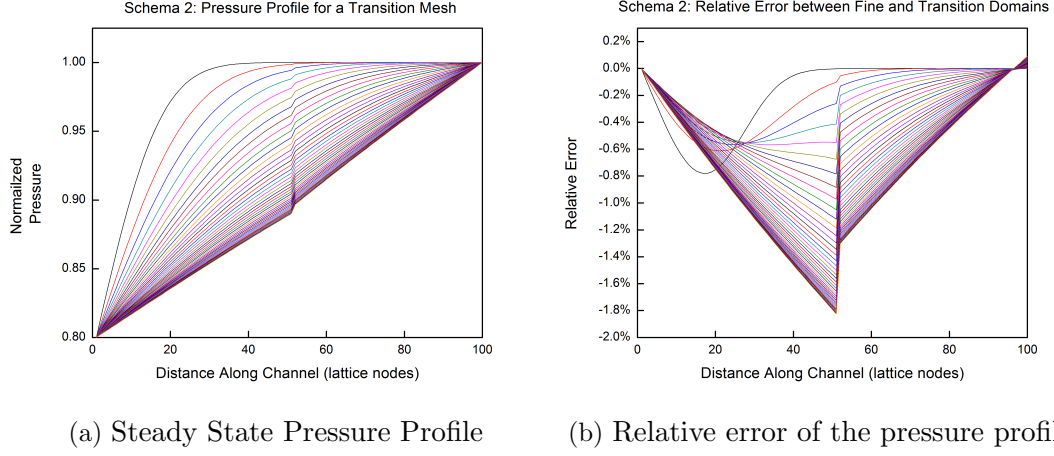


Figure 7.9: Pressure profile and relative error plots of a transition mesh using Schema 2 are shown in Fig.(a) and (b). Each line represents the pressure profile at intervals of 100 iteration steps.

a result of scaling only the equilibrium distribution function and assuming that the non-equilibrium distribution function is negligible, significant error arises, shown in Fig. 7.9b.

The last scheme to be tested for scaling distribution functions is Schema 3. Schema 3 is an extension of the Zou-He boundary condition [32]. Shown in Fig. 7.10a, Schema 3 does not appear to conserve mass for this test case, as evidenced by formation of a kink in the pressure profile. Fig.7.10b measures the extent of this error.

A more robust test for correctness can be performed using the recovery factor as a measure for comparison. While small deviations in pressure at a single node may seem insignificant, the sum deviation across all nodes compounds errors. Fig. 7.11 shows the recovery factor for a variety of mesh types: fine, coarse, and the 3 multi-domain schemes.

For the steady state case, the current implementation of a multi-domain mesh

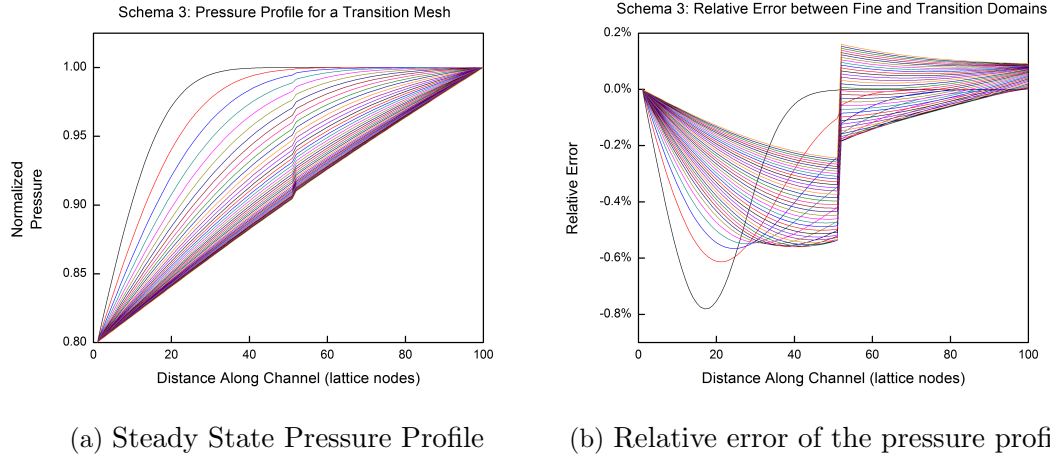


Figure 7.10: Pressure profile and relative error plots of a transition mesh using Schema 3 are shown in Fig.(a) and (b). Each line represents the pressure profile at intervals of 100 iteration steps.

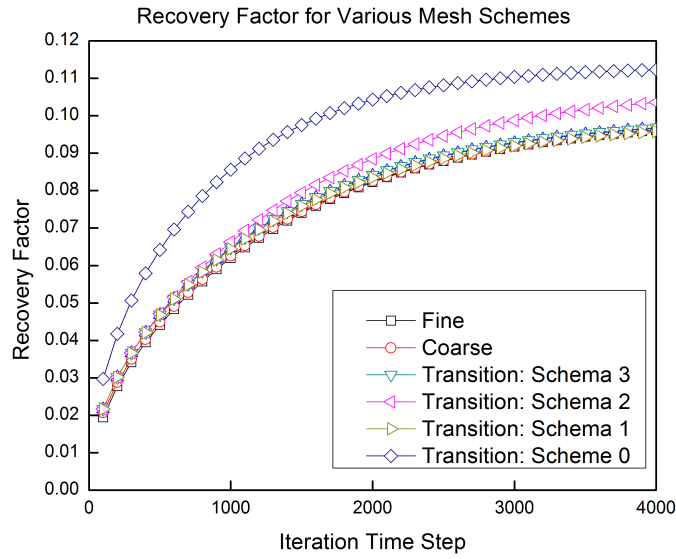


Figure 7.11: Plot of recovery factors using a variety of mesh schemes. Schema 1 provides recovery factor results that are closest to expected result.

(Schema 1) yields early time deviation in recovery factor from the fine mesh results. As time progresses and the system approaches steady state condition, the deviation in recovery factor minimizes, and approaches zero.

To conclude the 2D channel flow convective refinement results section, the results show that scaling the equilibrium and the non-equilibrium functions provide the most accurate result.

### *7.5.3 Convergence Analysis of a 2D Channel Pseudo Steady State Flow*

A convergence test is required on the 2D Channel undergoing a pseudo steady state flow before a multi-domain simulation is run. Once two successive levels of refinement converge to a solution, those two levels can be used for multi-domain gridding. The flow parameters used are the same as the ones used for the steady state tests, except at the outlet, where a no-flow boundary condition is imposed.

Fig. 7.12 are the convergence results. The relative error between the coarse and fine grids are low. This is a close match and validates that the coarse and fine simulation runs are near equivalent.

### *7.5.4 2D Channel Pseudo Steady State Flow Results*

In the previous simulation, there are two main sources of error. The first is our choice in how flow values are scaled. The second is from interpolation effects in the grid coupling algorithm. To further test the multi-domain approach and possible sources of error, the outlet boundary condition is changed to a no-flow boundary and Schema 1 is used to transfer distribution function information across mesh domains.

A no-flow boundary condition is more common to reservoir simulation and a better indicator of the accuracy of the Schema 1 method. Fig. 7.13a shows the evolution of the pressure field over time as the 2D channel is drained. The various plots are the pressure profile taken at every 100 iteration steps. An important characteristic

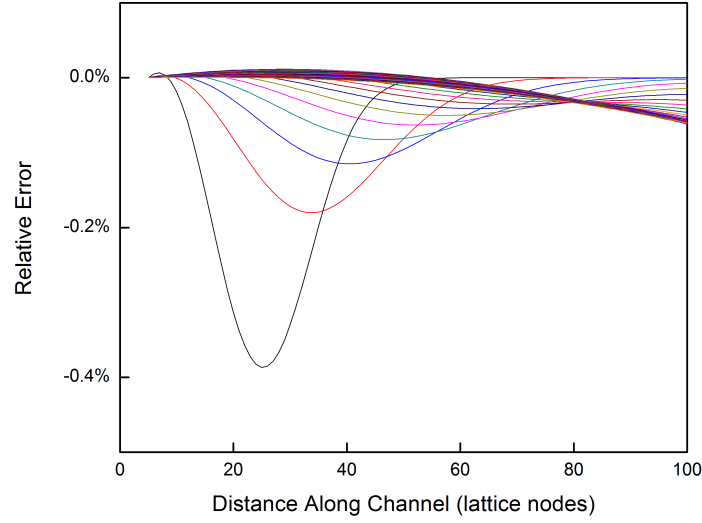
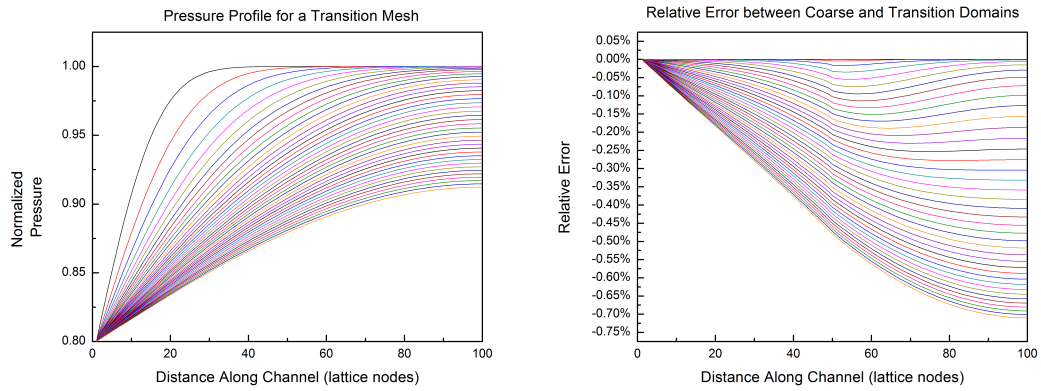


Figure 7.12: A convergence test between two mesh sizes, for a flow approaching a pseudo steady state solution. The size of the two meshes differs by a factor of 2. The relative error of the pressure profile along the channel is measured



(a) Psuedo steady pressure profile

(b) Relative error of pressure profile

Figure 7.13: Psuedo steady state 2D channel flow. Fig. (a) shows how the pressure field of a multi-domain mesh reduces over time as the 2D channel is drained. Fig. (b) is a plot of the relative error in the pressure field along the channel between the multi-domain mesh and the coarse only mesh.

of a multi-domain mesh is that the pressure appears continuous over the transition boundary. By inspection, the pressure plot is smooth along the transition zone (occurring at the 50 lattice unit mark). This suggests that our choice to convectively scale the system, as well as the interpolation of pressure and velocity from the coarse to the fine mesh is a valid approach.

Fig. 7.13b plots the relative error between the pressure profile of the Schema 1 multi-domain mesh and a coarse only mesh. The percent error as the simulation is allowed to run appears to converge at later times. This is different from the results of the steady state condition where the relative error converged and then minimized. As stated earlier, this was due to the tight bounds provided by the constant pressure condition at inlet and outlet. We would not expect the same for a psuedo steady state model. Viewing the relative error plot also shows the location of the transition zone. A small kink in the relative error plot reveals that some information is not properly scaled from one system to another. This kink could also represent the introduction of error due to the pressure and velocity interpolation.

#### 7.5.5 *Convergence Analysis of Homogenous Well Simulation Results*

For the 2D channel flow example, all nodes were aligned with the boundary and so a convective refinement scheme was sufficient. However, for radial flows where a large number of lattice nodes are not in line with the pressure boundary, a convective refinement technique will not be able to maintain simulation similarity. The inaccuracy of convective refinement for point source geometries is explored in this section.

The flow parameters for this study are  $Da = 0.00025$ ,  $J = 1$ ,  $\phi = 0.25$ .  $\tau_c = 5$  is set for the coarsest mesh and scaled according to convective scaling. Three levels of refined meshes are compared. The fine mesh simulated is 251 by 251 lattice nodes,

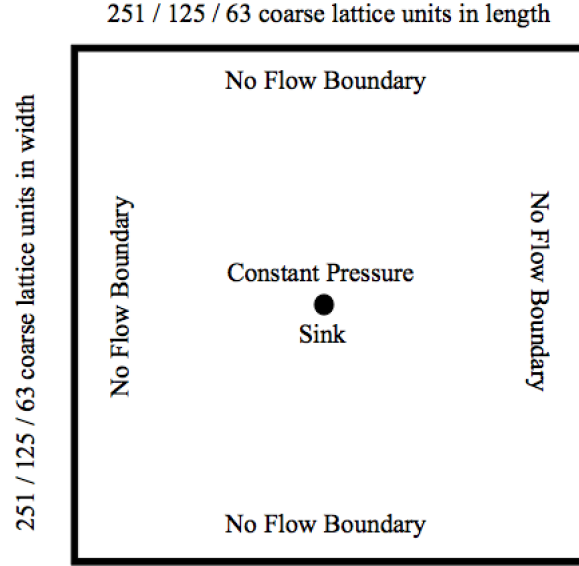


Figure 7.14: Geometry of a Homogenous Well Simulation. No flow boundaries along the edge of the domain. Constant pressure sink of 80% the initial reservoir pressure.

one level up is a mesh of 125 by 125 lattice nodes, and the coarsest mesh is 63 by 63 lattice nodes. The well or point source is located at the center of the domain. A constant pressure boundary condition is held at the source of 0.8 the initial reservoir pressure. The edge of the inner boundary condition has a radius of 0.2m from the center lattice point and so the pressure must be interpolated to that distance. The outer boundaries are set to have a no flow boundary condition.

The recovery factor over time is measured for each grid size, shown in Fig. 7.15. What this plot shows is that for successive levels of refinement, the recovery factor begins to diverge from previous solutions. The divergence is a result of the explanation given earlier: that we are using a convective refinement scheme where diffusive elements play a significant role in the evolution of the flow field. By using a convective refinement scheme, we are not properly scaling the diffusive elements at each



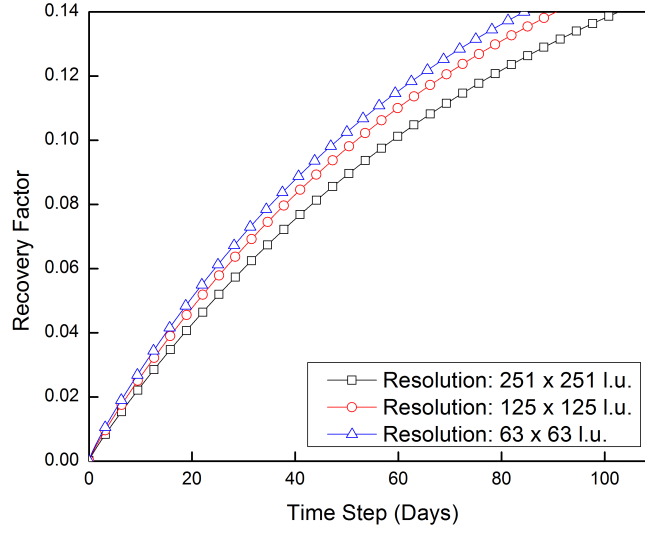


Figure 7.15: A convergence test between three mesh sizes, for a point source geometry approaching a pseudo steady state solution. The size of successively finer meshes differs by a factor of 2. The recovery factor of each simulation is measured. A divergence in expected solution results from a convective refinement scheme.

level of refinement. This divergence is a result of a constantly increasing diffusive force between levels of refinement.

## 7.6 Diffusive Refinement

Diffusive scaling was mentioned briefly in the discussion about temporal and spatial refinement. The scaling relation between the time step and spatial step in a diffusive refinement scheme is  $\delta t \propto \delta x^2$ . And so if we stick with the convention that  $x_f = x_c/2$ , then  $t_f = t_c/4$ . Parameter scaling needs to be updated to reflect diffusive scaling.

### 7.6.1 Rescaling Forcing Terms

Let us start with the Reynolds number. Using Eq. 7.3, a new scaling relation for the kinetic viscosity is formed.

$$Re_c = Re_f = \frac{UL\delta t_c}{\delta x_c^2 \nu_{e_c}} = \frac{UL\delta t_f}{\delta x_f^2 \nu_{e_f}} \quad (7.30)$$

$$\nu_{e_f} = \nu_{e_c} \quad (7.31)$$

Next, using the viscous number and the scale independence of kinematic viscosity terms, it can be shown that fluid viscosity is also scale independent, shown in Eq. 7.32 and 7.33.

$$J = \frac{\nu_{e_f}}{\nu_f} = \frac{\nu_{e_c}}{\nu_c} \quad (7.32)$$

$$\nu_f = \nu_c \quad (7.33)$$

Similarly, porosity is dimensionless and does not require scaling.

Lastly, since the permeability is only dependent on the level of spatial discretization, the scaling relation for permeability from in the previous section also holds.

### 7.6.2 Rescaling the Distribution Function

To scale the distribution function diffusively, let us first review the explicit version of the distribution function and walk through how to scale each term.

$$f_i = w_i \rho \left[ 1 + \frac{\mathbf{e}_i \cdot \mathbf{u}}{c_s^2} + \frac{\mathbf{u} \mathbf{u} : (\mathbf{e}_i \mathbf{e}_i - c_s^2 \mathbf{I})}{2c_s^4} \right] - \frac{w_i \rho}{c_s^2 \omega} \mathbf{Q}_i : \mathbf{S} \quad (7.34)$$

$$\mathbf{Q}_i = \mathbf{e}_i \mathbf{e}_i - c_s^2 \mathbf{I} \quad (7.35)$$

$$\mathbf{S} = \frac{1}{2} \left[ \nabla \mathbf{u} + (\nabla \mathbf{u})^T \right] \quad (7.36)$$

#### 7.6.2.1 Rescaling the Equilibrium Distribution Function

Shown again in Eq. 7.34, the equilibrium portion of the distribution function is dependent on lattice weights, density, damped velocity and the speed of sound of the lattice. The lattice weights are grid dependent and so for the D2Q9 grid scheme, the lattice weights go unchanged. The density is still a continuous field and independent of spatial and temporal discretization. The damped velocity and the speed of sound of the lattice requires rescaling.

The equation used in the convective scaling of the damped equation is still valid since no relationship between  $\delta t$  and  $\delta x$  has been imposed. Restating Eq. 7.20 and imposing the diffusive scaling between temporal and spatial discretization yields Eq. 7.37

$$\alpha = \frac{\delta x_f}{\delta x_c} \frac{\delta t_c}{\delta t_f} + \frac{\delta x_f}{\delta x_c} \frac{\nu_f}{\nu_c} \frac{K_c}{K_f} = \frac{17}{8} \quad (7.37)$$

Now that there is a scaling relation set for damped velocity, let's next check how

the speed of sound of the lattice is scaled through inspection of the temporal velocity.

$$v_f = \alpha v_c \quad (7.38)$$

Converting to a characteristic temporal velocity gives:

$$V \frac{\delta t_f}{\delta x_f} = \alpha V \frac{\delta t_c}{\delta x_c} \quad (7.39)$$

And rearranging:

$$\alpha = \frac{\delta t_c}{\delta t_f} \frac{\delta x_f}{\delta x_c} = 2 \quad (7.40)$$

Next, it is useful to introduce a new dimensionless number, called the Mach number. The Mach number is the ratio between a characteristic flow velocity and the speed of sound of the lattice, given by Eq. 7.41.

$$Ma = \frac{v_n}{c_s} \quad (7.41)$$

Using the Mach number, we must redefine the speed of sound of the lattice  $cs$  under the diffusive refinement scheme.

$$Ma = \frac{v_f}{cs_f} = \frac{v_c}{cs_c} \quad (7.42)$$

$$cs_f = 2cs_c \quad (7.43)$$

### 7.6.2.2 Rescaling the Non-Equilibrium Distribution Function

The explicit representation of the non-equilibrium portion of the distribution function is composed of lattice weights, the density, the speed of sound of the lattice,

the relaxation parameter  $\tau$ , and the gradient of the damped fluid velocity.

Mentioned previously, the lattice weights, and density are scale independent. The scaling for the speed of sound has already been defined. To scale the relaxation parameter, we use the equation of state that relates the kinetic viscosity of the fluid to the relaxation parameter. From the definition of kinematic viscosity under diffusive scaling:

$$\nu_f = \nu_c \quad (7.44)$$

$$cs_f^2(\tau_f - 1/2) = cs_c^2(\tau_c - 1/2) \quad (7.45)$$

Using the scaling equation defined for the lattice speed of sound along with Eq. 7.45 yields Eq. 7.46.

$$\tau_f = 1/4\tau_c - 3/2 \quad (7.46)$$

To ensure continuity of the non-equilibrium portion of the distribution function between mesh domains, we will modify Lagrava et al. [44] formulation to agree with diffusive scaling.

$$f_f^{neq} = \beta f_c^{neq} \quad (7.47)$$

$$\frac{w_i \rho \tau_c}{cs_c^2} \mathbf{Q}_i : \mathbf{S}_c = \beta \frac{w_i \rho \tau_f}{cs_f^2} \mathbf{Q}_i : \mathbf{S}_f \quad (7.48)$$

$$\frac{\tau_c}{cs_c^2 \delta t_c} \mathbf{Q}_i : \mathbf{S} = \beta \frac{\tau_f}{cs_f^2 \delta t_f} \mathbf{Q}_i : \mathbf{S} \quad (7.49)$$

$$\beta = \frac{\tau_c cs_f^2 \delta t_f}{\tau_f cs_c^2 \delta t_c} \quad (7.50)$$

#### 7.6.2.3 *Coupling from Fine to Coarse Grid*

The coupling of the distribution function from the fine to coarse grid is similar to that of the convective scheme. After the end of each coarse time step, there are unknown distribution functions that have streamed from outside the computational domain (from the fine domain). The unknown distribution functions can be solved for in a variety of ways as shown in the previous section. But since this is a diffusive grid refinement process, we need to properly scale higher order non-equilibrium terms of the distribution function so that momentum and mass is conserved across the transition zones.

To solve for the unknown distribution functions streaming into the coarse grid from the multi-domain boundary, information from the fine sites that overlay the coarse sites is needed. Using the methodology presented in the sections previous, the distribution functions are scaled to the coarse grid.

#### 7.6.2.4 *Coupling from Coarse to Fine Grid*

The method for transferring distribution information from the coarse to the fine grid takes a similar form as in the convective refinement. The major difference between the convective and diffusive technique for coupling the coarse to fine grid is the number of fine time steps that take place between each coarse time step. To temporally interpolate density and velocity values at fine time steps between time step  $t$  and  $t + \delta t_c$ , a linear interpolation is used. The unknown fine distribution functions are then solved for using the temporally and spatially interpolated density and velocity values of the coarse grid along with scaling techniques presented in

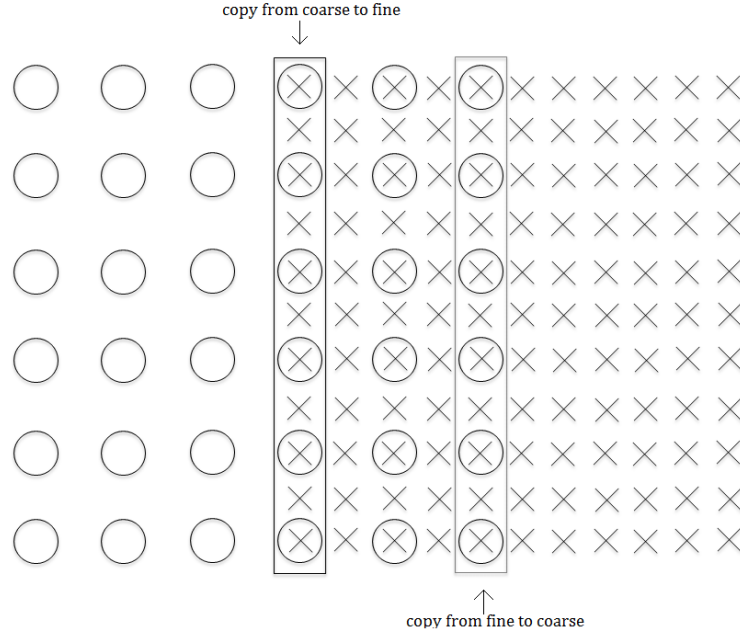


Figure 7.16: The transition zone between coarse and fine meshes in the diffusive flow regime. The sites labeled 'copy from coarse to fine' are the sites where distribution functions are scaled from the coarse grid to the fine grid. Sites labeled 'copy from fine to coarse' are the sites where information is scaled from the fine sites to coarse sites. The transition zone is three coarse lattice units wide. This is due to the squared relation in time and lattice spacing  $\delta t \propto \delta x^2$ . Twice the resolution requires four times as many time steps for diffusive flows.

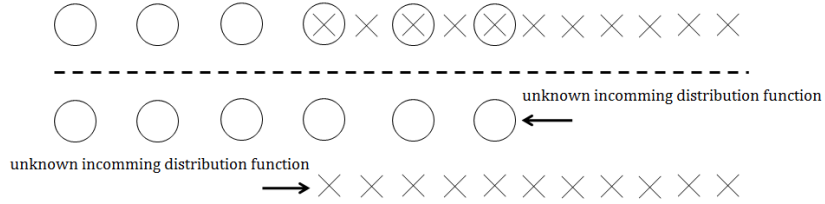


Figure 7.17: Above the dashed line is a 1D excerpt of a diffusive mesh. Below the dashed line is the fine and coarse lattice sites are separated to highlight the unknown distribution functions after each successive streaming step .

previous sections.

#### 7.6.2.5 Grid Coupling Algorithm

Again, we use the format presented by Lagrava et al. [44] to illustrate how a grid coupling algorithm is used for GLBM multi-domain meshes. Below are the steps required to pass information between meshes using the theory provided in previous sections under a diffusive refinement scheme.

1. A collide and stream operation is performed on the coarse grid, bringing the time to  $t + \delta t_c$ . At this time, distributions at coarse nodes that were supposed to stream from the fine grid are unknown.
2. A collide and stream operation is performed on the fine grid, bringing the time to  $t + \delta t_c/4$ . The grid lacks information at the transition sites from coarse to fine. A double interpolation is performed (time and space). First  $\mathbf{u}_c$  is scaled using 7.17. Then the values of  $\rho_c$  and  $\mathbf{u}_f$  of the coarse sites are interpolated at time  $t + \delta t_c/4$ . Then the time interpolated values, are interpolated in space to fine nodes that are not overlaid on coarse node sites. All distribution functions are solved using a schema appropriate to the application.
3. The previous set is repeated 2 more times.
4. On the last collide and stream operation, the time is brought to  $t + \delta t_c$ . No time interpolation is required during this step. Values for density and velocity are taken from step 1 and the velocity is scaled. A spatial interpolation is still required for off-coarse-node fine node lattice sites.
5. All populations of the coarse grid are updated using the schema of choice.



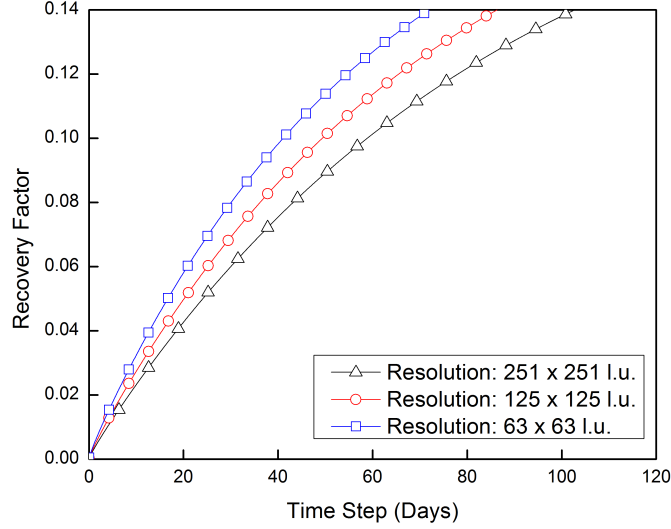


Figure 7.18: A convergence test between three mesh sizes, for a point source geometry approaching a pseudo steady state solution. The size of successively finer meshes differs by a factor of 2. The recovery factor of each simulation is measured. A constant offset in the expected solution forms as a result diffusive refinement.

## 7.7 Diffusive Grid Refinement Results

### 7.7.1 Convergence Analysis of Homogenous Well Simulation Results

To see the full effects of diffusive scaling, our first example is a point source geometry with no flow boundary conditions. Mentioned previously, the effects of diffusion are significant in systems where a large portion of the lattice nodes are not aligned radially to the source.

The flow geometry and the dimensionless flow parameters used are the same from the convective refinement results section of the same geometry.

Fig. 7.18 shows the recovery factor of three simulation runs at levels of refinement of 63x63, 125x125, and 251x251. A constant offset exists in the recovery factor of each run.

A possible reason for non-convergence is compressibility errors becoming significant. The choice in pressure differential from source to reservoir may approach the speed of sound of the lattice at finer levels of refinement and so a constant error forms.

## 8. CONCLUSIONS AND FINAL REMARKS

We started this research with a question: is it possible to improve the risk inherent to reservoir simulation? Through the development of alternative reservoir simulation tools and uncertainty models, the risk associated with improperly predicting future production can be mitigated. By looking at a problem through several lenses, the potential range of outcomes becomes well defined.

What has been shown through this research is that a lattice Boltzmann model for simulating flows through porous media at the REV scale produces results that align with conventional techniques, but also reveals interesting deviations. When a difference of 1% in production surmounts to a change in value on the order of millions of dollars, deviations become especially important to identify and understand.

The simulation of flows in unconventional reservoirs is a challenging endeavor. We began this work focusing on aspects we thought were most important. Capturing various flow regimes as well as fine grained heterogeneities in the matrix and fracture system were at the top of our list. Implementing a generalized lattice Boltzmann model addressed these issues first. The GLBM simulated a generalized Navier-Stokes equation, which included inertial, viscous and non-linear damping terms, necessary in the simulation of high flow rates in the fracture system, while the potential for parallel computation of the LBM lent itself to fine grained system resolution. Once these topics were addressed, the research began to fill in other necessities that commercial reservoir simulation tools offered. Local grid refinement and two phase flows were next on that check-list.

Although the LBM has been used extensively to simulate flows at the pore scale, application of the LBM to petroleum engineering problems is still in its infancy.

## 8.1 Discussion of Results

The results in this paper have been split into two sections, results on the development of the GLBM reservoir simulation tool, and results on the development of a grid refinement technique applied to the GLBM reservoir simulation tool.

For a homogenous and heterogenous well, it has been shown that the GLBM has recovered the macroscopic fluid equations (in this case the Darcy equation) in the incompressible limit. When compared against finite difference simulations of the same domain, the GLBM results are in great agreement. However, deviations occur in the tail end of the simulation for both homogenous and heterogeneous cases. This is the result of diffusive (viscous) forces becoming more significant at the end of the simulations life time. As a result of diffusive forces, the simulation smooths out over a longer period of time, thereby increasing the time for the reservoir to reach the steady state condition.

The influence of viscous forces on our these results can be mitigated by dynamically updating the relaxation parameter. When viscous forces are no longer needed for stability during early, high pressure differential, times, they can be lessened, resulting in a closer result to the expected Darcy solution.

For the case of local grid refinement, a convective scheme has been shown to work for 1D porous media flows along a channel. However, when a convergence analysis was performed prior to a convective grid refinement of a 2D homogenous well, convergence was not reached. Using a diffusive scheme instead, the convergence analysis was performed again. However, it has been shown that for the parameters used, convergence was not achieved in this case either.

As explained previously, the lattice Boltzmann equation is a mixed equation, where there is no set relation between time increment and spatial increment. There-

fore, using dimensionless numbers and a temporal/spatial grid refinement scheme does not yield the expected behavior for the 2D point source case. This issue in our results serves as an introduction to future work.

## 8.2 Opportunities for Further Research

### 8.2.1 *Grd Refinement*

Notwithstanding the demonstrated potential of a local grid refinement technique applied to the GLBM in 2D channel flows, issues with our results in the 2D point source geometries for convective and diffusive scaling have been identified. Neither convective nor diffusive scaling results in converged solutions.

Future work on grid refinement should start with identifying a relationship between spatial discretization and temporal discretization. This relationship can then be extended towards 2D point source geometries using the framework provided in the local grid refinement section.

### 8.2.2 *Two and Three Phase Porous Media Flow*

The lattice Boltzmann method has shown great potential in simulating multiphase flows. The Shan-Chen model has shown success in simulating semi-compressible and incompressible two phase flows [48, 49, 50]. Using the Shan-Chen model as a framework, the GLBM could potentially be extended to simulate water injection schemes at the field scale.

Instead of using the Shan-Chen model for simulating two phase fluids, an alternate approach would be to use the concept of relative permeability to simulate the presence of two phases. In order to implement such a model, a concept of saturation needs to be defined for the lattice system. Once saturation has been defined using distribution functions, we can then relate saturation to relative permeability in the same way most black-oil models simulate multiple phases. This concept of calculating relative

permeabilities based off of a lattice saturation can be further extended to include the gas phase.

A departure from the relative permeability concept for simulating a gaseous phase, Multi-Relaxation Time lattice Boltzmann models (MRT-LBM) have been developed to simulate compressible fluids [51]. So far, the GLBM has only included incompressible fluids. Using MRT-LBM as a starting point, we can include compressible fluids into the reservoir simulation suite.

### *8.2.3 Parallelization of GLBM and Comparison with Finite Difference Run Times*

One of the major draws of the lattice Boltzmann method is its simple parallelization of the code base. The collision step, which includes the diffusivity and damping terms, is a purely local function acting on a single lattice site. By parallelizing this section of the code to be computed on its own processor, the speed of simulation increases significantly. But by how much? There have been some studies that have modeled run times against number of processors used [41], but this does not give a comparative result to other more established reservoir simulation techniques.

A good step forward in validating the GLBM as a reservoir simulation tool would be to streamline and parallelize the codebase, then compare the run times of the GLBM to finite difference simulations using an increasing number of processors for each comparative run.

In addition, memory allocation is a significant issue in developing a commercial reservoir simulator. The GLBM requires that we store information about the distribution functions at each node. For a 2D simulation, this is a total of 9 pieces of information, where for a 3D simulation it is 19 pieces of information. This does not include permeability, porosity, or relaxation data. Compared against finite difference techniques, only pressure and saturation data are kept, again not including rock and

fluid data.

A robust analysis of run times and memory allocation would be a great extension to this current work, especially since the GLBM is in its infancy and requires significant development.

## REFERENCES

- [1] Securities and E. Commission, “Modernization of oil and gas reporting,” 2010.
- [2] L. Dake, *Fundamentals of Reservoir Engineering*. Amsterdam, The Netherlands: Elsevier BV., 1978.
- [3] G. King, “Thirty years of gas shale fracturing: What have we learned?,” *Society of Petroleum Engineers*, 2010.
- [4] N. Warpinski and L. Teufel, “Influence of geologic discontinuities on hydraulic fracture propagation,” *Journal of Petroleum Technology*, vol. 39, 1987.
- [5] C. H. Sondergeld, R. J. Ambrose, C. S. Rai, and J. Moncrieff, “Micro-structural studies of gas shales,” *Society of Petroleum Engineers*, 2010.
- [6] P. Forchheimer, “Wasserbewegung durch boden,” *Zeitschrift des Vereines Deutscher Ingenieuer*, 1901.
- [7] S. Anwar, *Lattice Boltzmann Modeling of Fluid Flow and Solute Transport in Karst Aquifers*. PhD thesis, FIU, 2008.
- [8] R. Liu, B. Li, and Y. Jiang, “Critical hydraulic gradient for nonlinear flow through rock fracture networks: The roles of aperture, surface roughness, and number of intersections,” *Advances in Water Resources*, vol. 88, pp. 53 – 65, 2016.
- [9] K. Aziz and A. Settari, *Petroleum Reservoir Simulation*. Applied Science Publishers Ltd, 1979.
- [10] A. Zidane and A. Firoozabadi, “An efficient numerical model for multicomponent compressible flow in fractured porous media,” *Advances in Water Resources*, vol. 74, pp. 127 – 147, 2014.
- [11] J. Moortgat and A. Firoozabadi, “Higher-order compositional modeling with



- fickian diffusion in unstructured and anisotropic media,” *Advances in Water Resources*, vol. 33, no. 9, pp. 951 – 968, 2010.
- [12] M. McClure, M. Babazadeh, S. Shiozawa, and J. Huang, “Fully coupled hydromechanical simulation of hydraulic fracturing in 3d discrete-fracture networks,” *SPE Journal*, 2016.
  - [13] M. Mayerhofer, E. Lolon, J. Youngblood, and J. Heinze, “Integration of microseismic-fracture-mapping results with numerical fracture network production modeling in the barnett shale,” *Presented at the SPE Annual Technical Conference and Exhibition, San Antonio, Texas*, 2006.
  - [14] C. Cipolla, E. Lolon, J. Erdle, and B. Rubin, “Reservoir modeling in shale-gas reservoirs,” *SPE Journal*, 2010.
  - [15] G. Fuentes-Cruz, E. Gildin, and P. Valk, “Analyzing production data from hydraulically fractured wells: The concept of induced permeability field,” *Society of Petroleum Engineers*, 2014.
  - [16] S. Succi, *The Lattice Boltzmann Equation*. Oxford University Press, 2001.
  - [17] D. Kandhai, A. Koponen, A. Hoekstra, M. Kataja, J. Timonen, and P. Slood, “Lattice-boltzmann hydrodynamics on parallel systems,” *Computer Physics Communications*, vol. 111, 1998.
  - [18] L. Laniewski-Wollk and J. Rokicki, “Adjoint lattice boltzmann for topology optimization on multi-gpu architecture,” *Computers and Mathematics with Applications*, 2016.
  - [19] O. Dardis and J. McCloskey, “Lattice boltzmann scheme with real numbered solid density for the simulation of flow in porous media,” *Phys. Rev. E*, vol. 57, pp. 4834–4837, Apr 1998.
  - [20] M. A. A. Spaid and F. R. Phelan, “Lattice boltzmann methods for modeling microscale flow in fibrous porous media,” *Physics of Fluids*, vol. 9, no. 9,

- pp. 2468–2474, 1997.
- [21] D. M. Freed, “Lattice-boltzmann method for macroscopic porous media modeling,” *International Journal of Modern Physics C*, vol. 09, no. 08, pp. 1491–1503, 1998.
  - [22] Z. Gou and T. Zhao, “Lattice boltzmann model for incompressible flows through porous media,” *Physical Review*, vol. E 66, 2002.
  - [23] L. Boltzmann, *Lectures on Gas Theory*. University of California Press, 1964.
  - [24] D. A. Wolf-Gladrow, *Lattice-Gas Cellular Automata and Lattice Boltzmann Models*. Springer-Verlag Berlin Heidelberg, 2000.
  - [25] P. L. Bhatnagar, E. P. Gross, and M. Krook, “A model for collision processes in gases. i. small amplitude processes in charged and neutral one-component systems,” *Phys. Rev.*, vol. 94, pp. 511–525, May 1954.
  - [26] S. Chapman and T. G. Cowling, *The mathematical theory of non-uniform gases: an account of the kinetic theory of viscosity, thermal condition, and diffusion in gases*. Cambridge University Press, 1960.
  - [27] S. Succi, E. Foti, and F. Higuera, “Three-dimensional flows in complex geometries with the lattice boltzmann method,” *EPL (Europhysics Letters)*, vol. 10, no. 5, p. 433, 1989.
  - [28] G. Punzo, F. Massaioli, and S. Succi, “High-resolution lattice-Boltzmann computing on the IBM SP1 scalable parallel computer,” *Computers in Physics*, vol. 8, pp. 705–711, Nov. 1994.
  - [29] K. Nordahl and P. S. Ringrose, “Identifying the representative elementary volume for permeability in heterolithic deposits using numerical rock models,” *Mathematical Geosciences*, vol. 40, no. 7, pp. 753–771, 2008.
  - [30] Z. Guo, C. Zheng, and B. Shi, “Discrete lattice effects on the forcing term in the lattice boltzmann method,” *Phys. Rev. E*, vol. 65, p. 046308, Apr 2002.

- [31] P. Lallemand and L.-S. Luo, “Theory of the lattice boltzmann method: Dispersion, dissipation, isotropy, galilean invariance, and stability,” *Phys. Rev. E*, vol. 61, pp. 6546–6562, Jun 2000.
- [32] Q. Zou and X. He, “On pressure and velocity boundary conditions for the lattice boltzmann bgk model,” *American Institute of Physics: Physics of Fluids*, 1997.
- [33] C. Wolowicz, J. B. Jr., and W. Gilbert, “Similitude requirements and scaling relationships as applied to model testing,” tech. rep., NASA, 1979.
- [34] S. of Petroleum Engineers, “Spe comparative solution project,” 2001.
- [35] T. Perkins, L. Kern, *et al.*, “Widths of hydraulic fractures,” *Journal of Petroleum Technology*, vol. 13, no. 09, pp. 937–949, 1961.
- [36] J. Geertsma, F. De Klerk, *et al.*, “A rapid method of predicting width and extent of hydraulically induced fractures,” *Journal of Petroleum Technology*, vol. 21, no. 12, pp. 1–571, 1969.
- [37] H. Kazemi *et al.*, “Pressure transient analysis of naturally fractured reservoirs with uniform fracture distribution,” *Society of petroleum engineers Journal*, vol. 9, no. 04, pp. 451–462, 1969.
- [38] H. Gerke and M. V. Genuchten, “A dual-porosity model for simulating the preferential movement of water and solutes in structured porous media,” *Water resources research*, vol. 29, no. 2, pp. 305–319, 1993.
- [39] S. R. Pride and J. G. Berryman, “Linear dynamics of double-porosity dual-permeability materials. i. governing equations and acoustic attenuation,” *Physical Review E*, vol. 68, no. 3, p. 036603, 2003.
- [40] P. Bailey, J. Myre, S. D. C. Walsh, D. J. Lilja, and M. O. Saar, “Accelerating lattice boltzmann fluid flow simulations using graphics processors,” in *2009 International Conference on Parallel Processing*, pp. 550–557, Sept 2009.
- [41] G. Wellein, T. Zeiser, G. Hager, and S. Donath, “On the single processor perfor-

- mance of simple lattice boltzmann kernels,” *Computers & Fluids*, vol. 35, no. 8, pp. 910–919, 2006.
- [42] S. Chen and G. D. Doolen, “Lattice boltzmann method for fluid flows,” *Annual review of fluid mechanics*, vol. 30, no. 1, pp. 329–364, 1998.
- [43] M. Christie, M. Blunt, *et al.*, “Tenth spe comparative solution project: A comparison of upscaling techniques,” in *SPE Reservoir Simulation Symposium*, Society of Petroleum Engineers, 2001.
- [44] D. Lagrava, O. Malaspinas, J. Latt, and B. Chopard, “Advances in multi-domain lattice boltzmann grid refinement,” *Journal of Computational Physics*, vol. 231, no. 14, pp. 4808 – 4822, 2012.
- [45] P. Sagaut, S. Deck, and M. Terracol, *Multiscale and multiresolution approaches in turbulence: LES, DES and hybrid RANS/LES methods: applications and guidelines*. World Scientific, 2013.
- [46] D. Lagrava, O. Malaspinas, J. Latt, and B. Chopard, “Automatic grid refinement criterion for lattice boltzmann method,” *arXiv preprint arXiv:1507.06767*, 2015.
- [47] J. Latt, “Choice of units in lattice boltzmann simulations,” *Freely available online at [http://lbmethod.org/\\_media/howtos: lbunits. pdf](http://lbmethod.org/_media/howtos:lbunits.pdf)*, 2008.
- [48] X. Shan and H. Chen, “Lattice boltzmann model for simulating flows with multiple phases and components,” *Physical Review E*, vol. 47, no. 3, p. 1815, 1993.
- [49] J. Chin, “Lattice boltzmann simulation of the flow of binary immiscible fluids with different viscosities using the shan-chen microscopic interaction model,” *Philosophical Transactions of the Royal Society of London A: Mathematical, Physical and Engineering Sciences*, vol. 360, no. 1792, pp. 547–558, 2002.
- [50] T. Inamuro, T. Ogata, S. Tajima, and N. Konishi, “A lattice boltzmann method

for incompressible two-phase flows with large density differences,” *Journal of Computational Physics*, vol. 198, no. 2, pp. 628–644, 2004.

- [51] D. d’Humières, “Multiple-relaxation-time lattice boltzmann models in three dimensions,” *Philosophical Transactions of the Royal Society of London A: Mathematical, Physical and Engineering Sciences*, vol. 360, no. 1792, pp. 437–451, 2002.

## APPENDIX A

### NON DIMENSIONALIZATION OF GOVERNING EQUATIONS

#### A.1 Non Dimensionalization of the Generalized Navier-Stokes Equation

Equations A.1.1 and A.1.2 represent the set of non-dimensional system parameters used in the non-dimensionlization of the governing macroscopic fluid equation, shown in Eq. A.1.3. The dimensionless variables are formed through the reference of a characteristic system variable, which can be found in the text of this paper.

$$r_d = r_p/r_{0,p}, \quad t_d = t_p/t_{0,p}, \quad u_d = u_p/u_{0,p} \quad (\text{A.1.1})$$

$$\nabla_d = r_{0,p} \nabla_p, \quad \nabla_d^2 = r_{0,p}^2 \nabla_p^2, \quad P_d = \frac{P_p}{\mu_e \frac{u_{0,p}}{r_{0,p}}} \quad (\text{A.1.2})$$

$$\frac{\partial \mathbf{u}}{\partial t} + \nabla \cdot \left( \frac{\mathbf{u}\mathbf{u}}{\phi} \right) = -\frac{1}{\rho} \nabla P + \nu_e \nabla^2 \mathbf{u} - \frac{\phi \nu}{K} \mathbf{u} \quad (\text{A.1.3})$$

After substitution of Eq. A.1.1 and A.1.2 into Eq. A.1.3:

$$\frac{u_{0,p}}{t_{0,p}} \frac{\partial u_d}{\partial t_d} + \frac{u_{0,p}^2}{r_{0,p}} \nabla_d \cdot \frac{u_d u_d}{\phi} = -\frac{\nu_e u_{0,p}}{r_{0,p}^2} \nabla_d P_d + \frac{\nu_e u_{0,p}}{r_{0,p}^2} \nabla_d^2 u_d - \frac{\nu u_{0,p}}{K} \phi u_d \quad (\text{A.1.4})$$

Each accelerating element within Eq. A.1.4 is composed of a group of characteristic system parameters and a non-dimensional group, which is of the order 1 everywhere within the flow field. The relative magnitudes of these forces (accelerating elements) are dictated by the characteristic system parameter group. These

coefficients have units of *length / time*<sup>2</sup>. We therefore can compare the relative magnitudes of each forcing element to one another to determine the dominating flow regime.

Let us compare the relative magnitude of the viscous force, given by  $\nu_e u_{0,p}/r_{0,p}^2$  in Eq. A.1.4 to all other elements by dividing throughout by the viscous coefficient.

$$\frac{u_{0,p} r_{0,p}}{\nu_e} \frac{r_{0,p}}{u_{0,p} t_{0,p}} \frac{\partial u_d}{\partial t_d} + \frac{u_{0,p} r_{0,p}}{\nu_e} \nabla_d \cdot \frac{u_d u_d}{\phi} = -\nabla_d P_d + \nabla_d^2 u_d - \phi \frac{\nu}{\nu_e} \frac{r_{0,p}^2}{K} \quad (\text{A.1.5})$$

$$\frac{Re}{St} \frac{\partial u_d}{\partial t_d} + Re \nabla_d \cdot \frac{u_d u_d}{\phi} = -\nabla_d P_d + \nabla_d^2 u_d - \frac{\phi}{J Da} u_d \quad (\text{A.1.6})$$

$$Re = \frac{u_{0,p} r_{0,p}}{\nu_e}, \quad J = \frac{\nu_e}{\nu}, \quad Da = \frac{K}{r_{0,p}^2} \quad (\text{A.1.7})$$

$$\phi = \frac{\text{pore volume}}{\text{total volume}}, \quad St = \frac{t_{0,p} u_{0,p}}{r_{0,p}} \quad (\text{A.1.8})$$

## A.2 Non Dimensionalization of the Continuity Equation

$$\frac{\partial}{\partial t}(\rho\phi) = -\nabla \cdot (\rho u) \quad (\text{A.2.1})$$

By substituting in the Darcy correlation for fluid velocity in porous media,

$$\frac{\partial}{\partial t}(\rho\phi) = -\nabla \cdot \left( \frac{K}{\nu} (\nabla P) \right) \quad (\text{A.2.2})$$

Using the variable assignments in A.1 and  $\rho_d = \rho_p / \rho_{0,p}$ , where  $\rho_{0,p}$  is a characteristic system density, a simple substitution yeilds:

$$\frac{\rho_{0,p}}{t_{0,p}} \frac{\partial}{\partial t_d} (\phi \rho_d) = -\frac{K}{\nu} \frac{\mu u_{0,p}}{r_{0,p}} \frac{1}{r_{0,p}^2} \cdot \nabla^2(P_d) \quad (\text{A.2.3})$$

By dividing the above equation throughout by the coefficient of the time dependent term, we arrive at the following:

$$\frac{\partial}{\partial t_d} (\phi \rho_d) = -\frac{K}{r_{0,p}^2} \frac{u_{0,p} t_{0,p}}{r_{0,p}} \cdot \nabla^2(P_d) \quad (\text{A.2.4})$$

$$\frac{\partial}{\partial t_d} \rho_d = -\frac{1}{\phi} Da St \cdot \nabla^2(P_d) \quad (\text{A.2.5})$$



## APPENDIX B

### MODIFIED ZOU-HE BOUNDARY FORMULATION

We assume that the bounce-back condition is valid for the non-equilibrium part of the distribution functions, given by Eqs. B.0.1 - B.0.3 [32].

$$f_3 = f_1 + f_3^{eq} - f_1^{eq} \quad (\text{B.0.1})$$

$$f_4 = f_2 + f_4^{eq} - f_2^{eq} \quad (\text{B.0.2})$$

$$f_7 = f_5 + f_7^{eq} - f_5^{eq} \quad (\text{B.0.3})$$

If we solve for the equilibrium contributions in Eqs. B.0.1 - B.0.3 using Eq. 3.6, Eqs. B.0.4 - B.0.6 are formed.

$$f_3 = f_1 - \frac{2}{3}\rho u_x \quad (\text{B.0.4})$$

$$f_4 = f_2 - \frac{2}{3}\rho u_y \quad (\text{B.0.5})$$

$$f_7 = f_5 - \frac{1}{6}(\rho u_x + \rho u_y) \quad (\text{B.0.6})$$

By the definition of  $\rho$  we have:

$$\rho = f_0 + f_1 + f_2 + f_3 + f_4 + f_5 + f_6 + f_7 + f_8 \quad (\text{B.0.7})$$

Further substitution of Eqs. B.0.4 - B.0.6 into Eq. B.0.7 leads to Eq. B.0.8:

$$\rho u_x + \rho u_y = -\frac{6}{5} \left( \rho - (f_0 + f_6 + f_8 + 2(f_1 + f_2 + f_5)) \right) \quad (\text{B.0.8})$$

Next, we will employ the definition of the temporal macroscopic velocity, given by Eq. 3.9.

$$\rho u_x = f_1 - f_3 + f_5 - f_7 + f_8 - f_6 \quad (\text{B.0.9})$$

Through the substitution of Eqs. B.0.4 - B.0.6 into Eq.B.0.9, we form Eq. B.0.10.

$$\rho u_x - \rho u_y = 6(f_8 - f_6) \quad (\text{B.0.10})$$

Now, all the relevant information has been derived to solve for  $f_3$ ,  $f_4$ , and  $f_7$ . The rearrangement and combination of Eqs. B.0.8 and B.0.10 yield:

$$f_3 = f_1 + \frac{2}{5} \left( \rho - (f_0 + f_6 + f_8 + 2(f_1 + f_2 + f_5)) \right) + 2(f_6 - f_8) \quad (\text{B.0.11})$$

$$f_4 = f_2 + \frac{2}{5} \left( \rho - (f_0 + f_6 + f_8 + 2(f_1 + f_2 + f_5)) \right) + 2(f_8 - f_6) \quad (\text{B.0.12})$$

$$f_7 = f_5 + \frac{1}{5} \left( \rho - (f_0 + f_6 + f_8 + 2(f_1 + f_2 + f_5)) \right) \quad (\text{B.0.13})$$

## APPENDIX C

### SPE-10 PERMEABILITY AND POROSITY FIELD

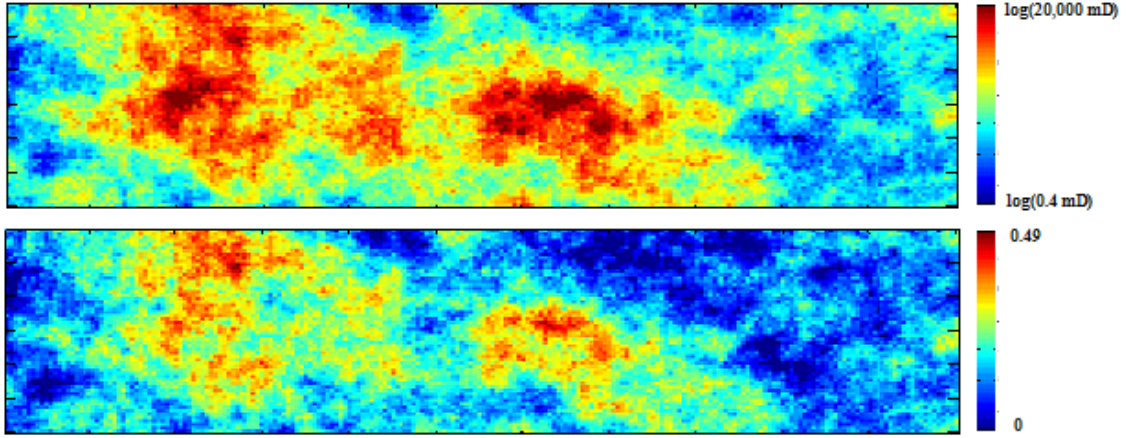


Figure C.0.1: SPE-10 Permeability (top) and porosity (bottom) data. Permeability values are scaled logarithmically for viewing. SPE-10 data is used to compare the generalized LBM with commercial simulation software. The 10th layer of the permeability and porosity field were used for simulation of 2D reservoir.

## APPENDIX D

### MODIFIED ZOU-HE BOUNDARY FORMULATION EXTENDED

We assume that the bounce-back condition is valid for the non-equilibrium part of the distribution functions, given by Eqs. B.0.1 - B.0.3 [32].

$$f_3 = f_1 + f_3^{eq} - f_1^{eq} \quad (\text{D.0.1})$$

$$f_4 = f_2 + f_4^{eq} - f_2^{eq} \quad (\text{D.0.2})$$

$$f_7 = f_5 + f_7^{eq} - f_5^{eq} \quad (\text{D.0.3})$$

If we solve for the equilibrium contributions in Eqs. D.0.1 - D.0.3 using Eq. 3.6, Eqs. D.0.4 - D.0.6 are formed.

$$f_3 = f_1 - \frac{2}{3}\rho u_x \quad (\text{D.0.4})$$

$$f_4 = f_2 - \frac{2}{3}\rho u_y \quad (\text{D.0.5})$$

$$f_7 = f_5 - \frac{1}{6}(\rho u_x + \rho u_y) \quad (\text{D.0.6})$$

By the definition of  $\rho$  we have:

$$\rho = f_0 + f_1 + f_2 + f_3 + f_4 + f_5 + f_6 + f_7 + f_8 \quad (\text{D.0.7})$$

Further substitution of Eqs. D.0.4 - D.0.6 into Eq. D.0.7 leads to Eq. D.0.8:

$$\rho u_x + \rho u_y = -\frac{6}{5} \left( \rho - (f_0 + f_6 + f_8 + 2(f_1 + f_2 + f_5)) \right) \quad (\text{D.0.8})$$

By substituting Eq. D.0.7 into Eq. D.0.8, we can solve for the unknown  $f_7$ , given in Eq. D.0.9

$$f_7 = f_5 + \frac{1}{5} \left( \rho - (f_0 + f_6 + f_8 + 2(f_1 + f_2 + f_5)) \right) \quad (\text{D.0.9})$$

Next, we will employ the definition of the damped macroscopic velocity, given by Eq. D.0.10 to solve for the unknown  $f_3$ .

$$\rho u_x = C \left( f_1 - f_3 + f_5 - f_7 + f_8 - f_6 \right) \quad (\text{D.0.10})$$

where C is the Darcy coefficient given in Eq. D.0.11

$$C = \frac{1}{1 + \frac{\phi \delta_t \nu}{2K}} \quad (\text{D.0.11})$$

By substituting D.0.10 and Eq. D.0.9 into Eq. D.0.4, with some algebraic manipulation, we arrive at Eq. D.0.12

$$f_3 = \frac{1}{1 - 2/3C} \left( f_1 + \frac{2C}{15} (\rho - f_0 - 2(f_2 + f_5) - 6f_8 + 4f_6 - 7f_1) \right) \quad (\text{D.0.12})$$

Next, we can solve for the unknown  $f_4$ , using the definition of damped velocity in the y direction, given by Eq. D.0.13.

$$\rho u_y = C \left( f_2 + f_5 + f_6 - f_4 - f_7 - f_8 \right) \quad (\text{D.0.13})$$

By substituting Eq. D.0.13 and Eq. D.0.9 into Eq. D.0.5, we can solve for  $f_4$  through some algebraic manipulation, given by Eq.D.0.14.

$$f_4 = \frac{1}{1 - 2/3C} \left( f_2 + \frac{2C}{15} (\rho - f_0 - 2(f_1 + f_5) - 6f_6 - 4f_8 - 7f_2) \right) \quad (\text{D.0.14})$$